iScience

CellPress
OPEN ACCESS

Article

The Division of Amyloid Fibrils: Systematic Comparison of Fibril Fragmentation Stability by Linking Theory with Experiments

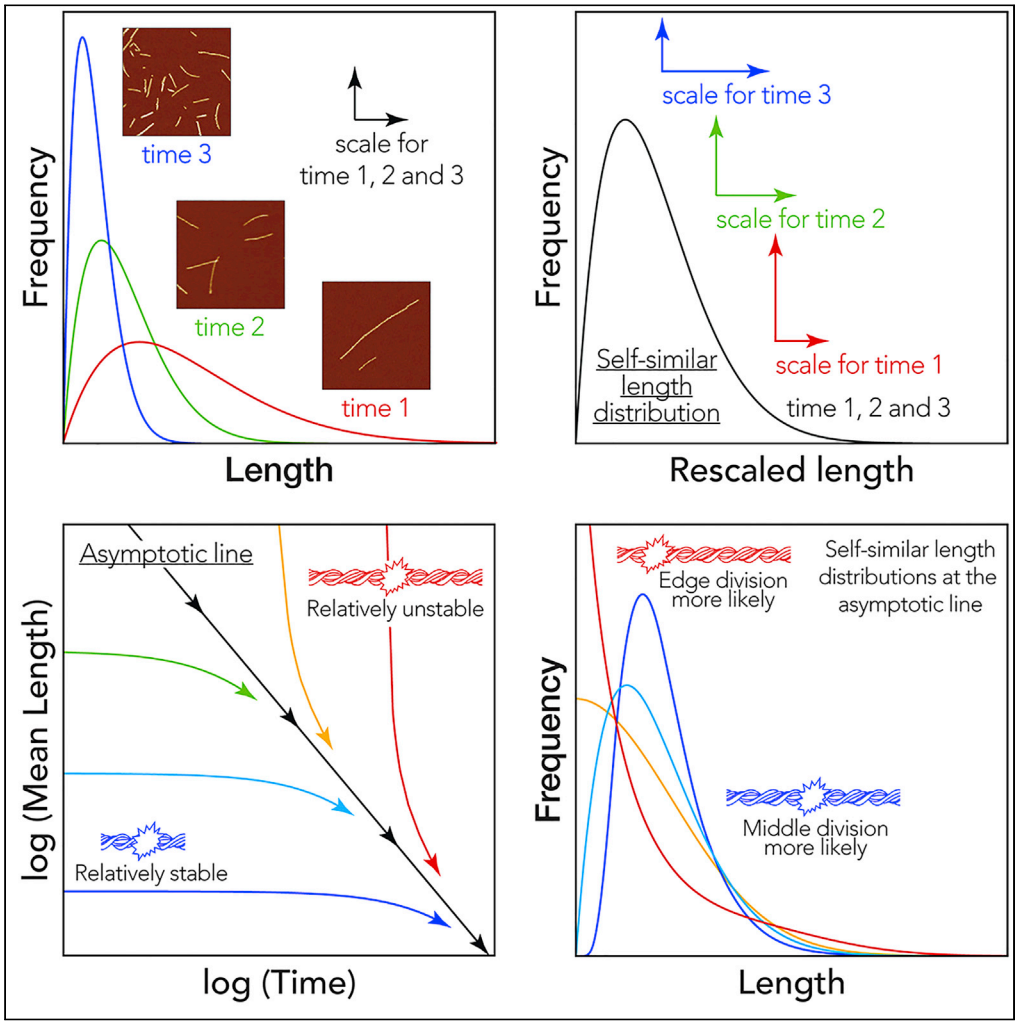

David M. Beal, Magali Tournus, Ricardo Marchante, ..., Mick F. Tuite, Marie Doumic, Wei-Feng Xue

w.f.xue@kent.ac.uk

HIGHLIGHTS

Theory on the division of amyloid fibrils developed using a continuous PDE framework

The theory allowed direct analysis of fibril breakage properties with AFM image data

The new insights enabled comparison of fibrils' intrinsic stability to breakage

α-Synuclein fibrils showed low stability to division compared with other model amyloid

Beal et al., iScience *23*, 101512
September 25, 2020
https://doi.org/10.1016/j.isci.2020.101512

iScience

CellPress
OPEN ACCESS

Article

The Division of Amyloid Fibrils: Systematic Comparison of Fibril Fragmentation Stability by Linking Theory with Experiments

David M. Beal,[1] Magali Tournus,[2] Ricardo Marchante,[1,6] Tracey J. Purton,[1] David P. Smith,[3] Mick F. Tuite,[1] Marie Doumic,[4,5] and Wei-Feng Xue[1,4,7,*]

SUMMARY

The division of amyloid protein fibrils is required for the propagation of the amyloid state and is an important contributor to their stability, pathogenicity, and normal function. Here, we combine kinetic nanoscale imaging experiments with analysis of a mathematical model to resolve and compare the division stability of amyloid fibrils. Our theoretical results show that the division of any type of filament results in self-similar length distributions distinct to each fibril type and the conditions applied. By applying these theoretical results to profile the dynamical stability toward breakage for four different amyloid types, we reveal particular differences in the division properties of disease-related amyloid formed from α-synuclein when compared with non-disease associated model amyloid, the former showing lowered intrinsic stability toward breakage and increased likelihood of shedding smaller particles. Our results enable the comparison of protein filaments' intrinsic dynamic stabilities, which are key to unraveling their toxic and infectious potentials.

INTRODUCTION

Amyloid fibrils, proteinaceous polymers with a cross-β core structure, represent an important class of bio-nanomaterials (Bleem and Daggett, 2017; Knowles and Buehler, 2011). They are also important biological structures associated with devastating human diseases such as Alzheimer disease, Parkinson disease, Creutzfeldt-Jakob disease, systemic amyloidosis, and type 2 diabetes (Knowles et al., 2014), as well as have vital biological functions such as adhesion and biofilm formation, epigenetic switches, and hormone storage (e.g., Berson et al., 2003; Bleem and Daggett, 2017; Chapman et al., 2002; Knowles and Buehler, 2011; Larsen et al., 2007; Li et al., 2014; Romero et al., 2010; Tuite and Serio, 2010). Division of amyloid fibrils, which can manifest *in vitro* in amyloid nanomaterials or *in vivo* in disease-associated or functional amyloid aggregates, is mediated by mechanical agitation, thermal stress, chemical perturbation, or chaperone catalysis. Fibril division is a crucial step in the life cycle of amyloid (Figure 1A) (Xue, 2015) and enables the propagation of the amyloid protein conformation and biological information encoded therein. Despite knowledge of its importance, it is not understood why amyloid division processes give rise to varied biological impacts ranging from normal propagation of functional amyloid assemblies to large inert structures or the creation of molecular species involved in disease, e.g., small cytotoxic amyloid species and infective prions, which are transmissible amyloid particles. In this respect, the resistance of amyloid to division is also a critical aspect to protein misfolding associated with disease progression and biological roles of functional amyloid assemblies (e.g., Tanaka et al., 2006). In terms of disease association, there is much debate as to how amyloid aggregates are associated with cellular toxicity, with evidence of both prefibrillar oligomers and fibrillar species (Breydo and Uversky, 2015; Tipping et al., 2015) giving rise to disease-related phenotypes. Although it is hypothesized that all proteins can undergo conversion into an amyloid state (Dobson, 1999), why most proteins do not form amyloid under physiological conditions or produce amyloid particles that are non-toxic, non-transmissible, or non-disease associated is not clear. In this debate, it has been suggested that fibrils are not merely the end product of amyloid aggregation, but rather elicit profound biological responses through fibril fragmentation and oligomer shedding (Tipping et al., 2015), due to lack of fibril stability.

Amyloid fibrils have remarkable physical properties, such as their tensile strength comparable to that of steel and elasticity similar to spider silk (Knowles et al., 2007). As proteinaceous polymers, they also offer

[1]Kent Fungal Group, School of Biosciences, University of Kent, CT2 7NJ Canterbury, UK

[2]Centrale Marseille, I2M, UMR 7373, CNRS, Aix-Marseille Univ., Marseille 13453, France

[3]Biomolecular Research Centre, Sheffield Hallam University, Sheffield, UK

[4]INRIA Rocquencourt, équipe-projet BANG, Domaine de Voluceau, BP 105, 78153 Rocquencourt, France

[5]Wolfgang Pauli Institute, University of Vienna, Vienna, Austria

[6]Present address: Institute for Genetics and CECAD Research Center, University of Cologne, Joseph-Stelzmann Str. 26, 50931 Cologne, Germany

[7]Lead Contact

*Correspondence: w.f.xue@kent.ac.uk

https://doi.org/10.1016/j.isci.2020.101512

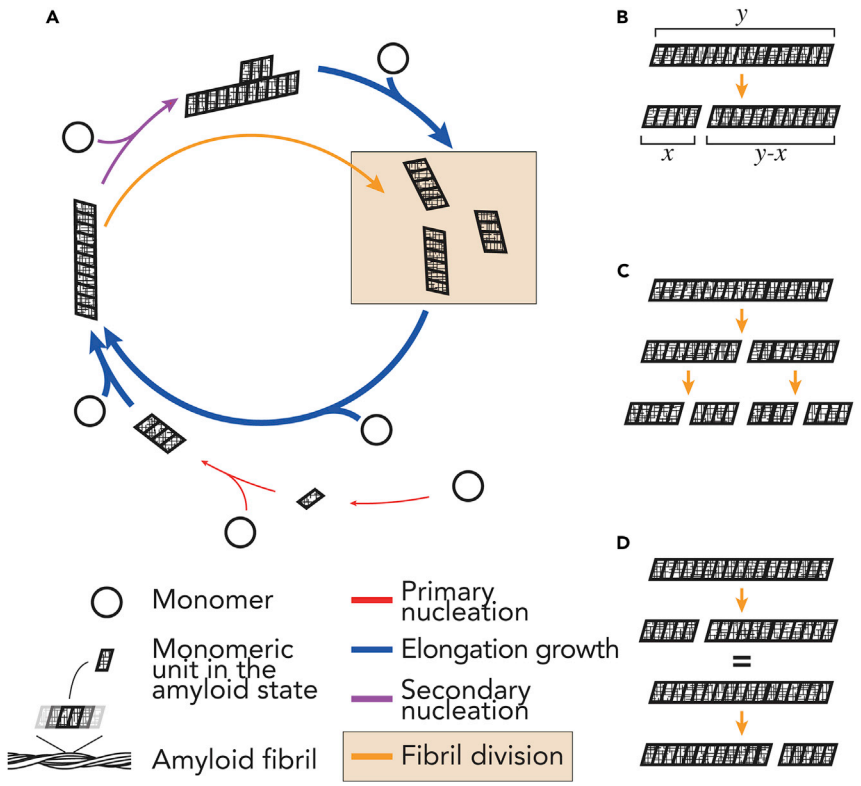

Figure 1. Schematic Illustration of Fibril Division in the Amyloid Life Cycle

(A) The life cycle of amyloid assembly where soluble monomeric proteins (circles) are converted into the amyloid state with a cross-β conformation (the parallelograms). The colored arrows represent the four main processes in amyloid assembly. Red arrows represent primary nucleation, which may occur as homogeneous nucleation in solution and heterogeneous nucleation at interfaces. Primary nucleation may also occur subsequent to liquid-liquid phase separation or phase transitions (Khan et al., 2018). Purple arrows represent secondary nucleation, which may occur as heterogeneous nucleation at surfaces presented by preformed aggregates. Blue arrows represent growth by elongation at fibril ends. Yellow arrows and box represent fibril division (e.g., fibril fragmentation or breakage). The arrows may represent consecutive reversible steps, and the thickness of the arrows symbolizes the relative rates involved in the processes.
(B) A simple model of fibril division, where a given parent fibril particle of length y divides to give rise to two daughter fibril particles of size x and y-x. The model does not otherwise identify the lineage of the individual fibrils.
(C) The division model assumes that each parent fibril particle divides into exactly two daughter particles at each microscopic reaction step.
(D) The division model assumes that the division rate for each microscopic step is identical as long as the resulting two particles have the same size.

the potential for modification by rational design, which makes them an ideal target for the development of biologically compatible nanomaterials (Bleem and Daggett, 2017; Hu et al., 2018; Li et al., 2014; Mankar et al., 2011). This interest in amyloid as a bio-nanomaterial has led to a search for proteins and peptides that can undergo conversion into a stable amyloid conformation while lacking the properties that associate them with toxicity, infectivity, and disease. Although the precise properties that associate some amyloid to disease or biological function are not resolved, the potential for different morphologies (sometimes referred to as "strains") to elicit different results (Meinhardt et al., 2009; Sachse et al., 2010; Tanaka et al., 2006) could be attributed to the stability of amyloid fibrils toward division or their mechanical properties (Marchante et al., 2017; Xue et al., 2009a). Thus, the stability of amyloid fibrils is an important physical factor that modulates their biological function of amyloid and potential as a nanomaterial.

The kinetics of the nucleated growth of amyloid fibrils are profoundly influenced by secondary processes such as fibril fragmentation/breakage (Knowles et al., 2009; Xue et al., 2008) and secondary surface nucleation (Buell et al., 2014; Tornquist et al., 2018) (Figure 1A). These processes determine the rate of the exponential growth phase of amyloid assembly alongside with growth by elongation at fibril ends (Lorenzen

et al., 2012; Xue et al., 2008). As one of the key secondary processes, fibril fragmentation stands out compared with the other three main processes (Figure 1A) in that it reduces the aggregate size at the same time as it increases the number of aggregates (Xue et al., 2009a). In this aspect, fibril fragmentation results in the division of amyloid fibrils analogous to a microbial or cellular division process. Resistance to fibril fragmentation is linked to the mechanical stability of amyloid fibrils, which has implications for both the development of nanomaterials and on the understanding of amyloid disease-associated biological processes. The mechanism and the rate of fibril fragmentation have been subjected to theoretical considerations (Hill, 1983; Knowles et al., 2009; Paparcone and Buehler, 2011; Xue et al., 2008) and experimental investigations involving fragmentation promoted by mechanical perturbations (Nicoud et al., 2015; Xue et al., 2008; Xue and Radford, 2013). The fragmentation of protein filaments is a length-dependent process whereby longer particles break more easily than short ones. This length-dependent breakage of amyloid fibrils can follow a strong, non-linear dependence where longer fibrils are progressively less stable toward breakage per monomeric unit relative to their shorter counterparts (Xue and Radford, 2013). Thus, the fibrils' resistance to division, and in turn the inherent stability of the fibrils, is an important and measurable property (Xue and Radford, 2013) that will help rationalize phenomena such as prion strains, polymorphism, transmission, amyloid toxicity, biofilm formation, and epigenetic regulation (e.g., Aguzzi et al., 2007; Cox et al., 2003; Derdowski et al., 2010; Lee et al., 2011; Lin et al., 2017; Marchante et al., 2017; Shorter and Lindquist, 2004; Sondheimer and Lindquist, 2000; Tanaka et al., 2006; Xue et al., 2009a; Zeng et al., 2015) and lead to a better understanding of amyloid-associated diseases.

The division of amyloid polymers into small more infective particles, either through environmental perturbations or through catalysis by molecular chaperones, is key to the spreading of prion phenotypes (Cox et al., 2003; Marchante et al., 2017). For example, the propagation of the yeast prion phenotype [PSI^+] associated with yeast Sup35 protein assemblies relies on the fragmentation activity of the chaperon Hsp104 and its co-chaperones (Chernoff et al., 1995; Shorter and Lindquist, 2004). The resistance of Sup35 assemblies to fragmentation correlates with the formation of different [PSI^+] phenotypes (Tanaka et al., 2006). In addition, the smaller particles generated by fibril fragmentation show enhanced cytotoxicity when compared with the larger parent fibrils (Xue et al., 2009a), likely due to a higher propensity to interact with cell membranes, entering cells by endocytosis, interacting with the lysosome, and inducing cytotoxicity by disrupting proteostasis (Ankarcrona et al., 2016; Hu et al., 2009; Jakhria et al., 2014; Marchante et al., 2017; Milanesi et al., 2012). The stability of amyloid fibrils toward division is, therefore, an important characteristic of amyloid fibrils that must be considered if we are to understand the biological activity and nanomaterial properties of amyloid. As protein filaments formed from different precursors show a variety of suprastructures and size distributions (e.g., Barritt et al., 2017; Knowles et al., 2007; Meinhardt et al., 2009; Xue et al., 2009a), no unifying theory has been developed for the division of amyloid fibrils. As consequence, the stability toward division for different types of amyloid fibrils with varied suprastructures that ranges from inert network of long filaments to infectious particles is yet to be systematically measured, determined, and compared.

We have previously shown that the time evolution of amyloid fibril length distributions obtained by nanoscale atomic force microscopy (AFM) imaging contain valuable information on the rate, length dependence, and position dependence of fibril fragmentation that can be extracted (Xue and Radford, 2013). However, as fibril division is itself a strongly length-dependent process, systematic comparison of the stability of fibrils toward division and their division rates has been hampered by the varied length distributions of different types of amyloid fibrils. Currently, the links between data and theory that would allow direct comparison of the fibrils' division propensities are also missing. Here, we have developed an analytical approach that enables direct determination of the dynamic stability of amyloid fibrils toward division from fibril length distributions. We have developed a new theory on amyloid fibril division that shows how the division mechanism of amyloid fibrils and their stability toward division dictates the exact shape of the resulting length distributions. We then established an analytical method to extract a set of unique and intrinsic properties of the fibril stability to division from image data of pre-formed fibrils undergoing physical fragmentation experimentally promoted by mechanical perturbation. Demonstrating the utility of our combined experimental and theoretical approach, we determined and compared the division of fibril samples formed from human α-synuclein (α-Syn) associated with Parkinson disease with fibrils formed from β-lactoglobulin (β-Lac) and lysozyme (Lyz). We have also reanalyzed and compared previously published fibril fragmentation data of β_2-microglobulin (β_2m) under the same mechanical perturbation regime (Xue and Radford, 2013). Comparison of the dynamic stability of these fibril types of different origin revealed different division properties, with fibrils formed from the human Parkinson disease-associated

α-Syn being the least overall stable and prone to generate small sub-100-nm particles that may possess enhanced cytotoxic and prion-like infectious potential (Brundin and Melki, 2017). The ability to assess and compare the division properties of amyloid fibrils, enumerated as parameters extractable from experimental data, enables the prediction of an amyloid's propensity to generate toxic and infectious particles and therefore has a significant impact on the understanding of their roles in biology, in diseases, and their application as a functional bio-nanomaterial.

RESULTS

Amyloid Fibrils of Diverse Suprastructures and Length Distributions Fragment to Different Extents upon Mechanical Perturbation

To demonstrate that the fibril division rates, indicative of their dynamic stability to division, can be assessed and compared for amyloid fibrils with diverse suprastructures and length distributions, we first collected experimental AFM image datasets of amyloid fibrils, pre-formed from different precursors, undergoing division through fragmentation promoted by mechanical stirring. These experiments were designed to isolate the fibril division processes from other growth processes and to generate data that contain sufficient quality and quantity of information on the division of fibril particles under identical mechanical perturbation regimes to enable comparison. Here, we chose to investigate the human disease-associated amyloid system α-Syn alongside bovine β-Lac and chicken egg white Lyz as biophysical model systems not directly related to human disease. Samples were formed containing long, straight fibrils from these three proteins *in vitro* and validated by negative-stain electron microscopic imaging (Figure S1). Lyz and β-Lac were both converted to their fibrillar amyloid form by heating under acidic conditions (pH 2.0), commonly used conditions for the assembly of these proteins *in vitro*. α-Syn fibrils were prepared from freshly purified recombinant α-Syn monomers (Cappai et al., 2005) at 37°C under physiological pH. For each fibril sample, 500 μL of 120 μM monomer equivalent fibril solutions in their respective fibril forming buffer were then stirred at 1,000 rpm by a 3 × 8-mm magnetic stirrer bar in a 1.5-mL glass chromatography vial using the same mechanical perturbation method as previously reported (Xue and Radford, 2013) with an Ika Squid stirrer plate with a digital display. The *in vitro*-formed fibril samples were initially dispersed by 5–10 min of stirring and were subsequently deposited onto freshly cleaved mica surfaces and imaged by AFM (Figure 2 leftmost column).

As seen in the leftmost column of images in Figure 2, the initial samples after brief stirring to disperse the fibril particles show long, straight, elongated, unbranched nanostructures expected for amyloid fibrils. However, whereas Lyz and α-Syn form fibrils that exhibit more flexibility and curvature, β-Lac forms comparably shorter, straighter, more rigid assemblies consistent with previous observations (e.g., Knowles et al., 2007; Lara et al., 2011; Nicoud et al., 2015; Sweers et al., 2012). The Lyz and β-Lac images also display higher background noise compared with the images of α-Syn fibrils, which may reflect their overall less-efficient fibril assembly reaction conditions compared with α-Syn. Importantly, however, all the samples showed well-dispersed fibril particles that can be individually measured after the brief stirring treatment, as the samples did not show strong propensity for clumping on the images.

The samples were then continuously stirred for up to 15 days, and 1–5 μL samples (see Transparent Methods) were taken out periodically and imaged using AFM to visualize their fragmentation under mechanical perturbation (Figure 2). For each sampling time point, an identical AFM specimen preparation procedure was used for each amyloid type, and 20 μm × 20 μm surface areas were imaged at 2,048 × 2,048-pixel resolution to enable quantitative analysis of individual fibril particles as previously described (Xue, 2013; Xue et al., 2009b). In total, fragmentation of two independent fibril samples was followed for each fibril type, and 171 images with at least 300 particles for each sample and time point were analyzed, giving a total dataset containing physical measurements of more than 220,000 individual fibril particles for the three amyloid types (Table S1).

Quantitative single-particle measurements of fibril length and height distributions (Figure 3, leftmost column corresponding to images in Figure 2 leftmost column) reveal that the fibrils have substantially different initial dimensions. Analysis of their height distributions shows that the initial fibril heights, indicative of the width of the fibrils, are around 7 nm for α-Syn fibrils and around 3 nm for both β-Lac and Lyz fibrils. The initial length distributions for the different fibril types were also dissimilar, with both Lyz and α-Syn forming fibrils of up to ~10 μm in length, whereas β-Lac formed shorter particles with lengths of up to ~2 μm under the conditions employed.

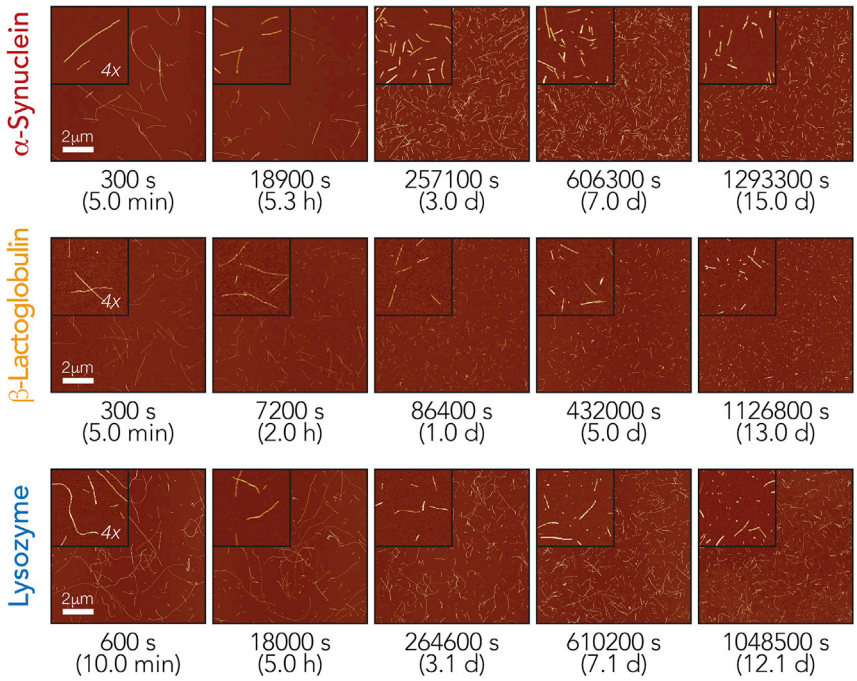

Figure 2. AFM Imaging of Amyloid Fibrils Undergoing Fragmentation Promoted by Mechanical Stirring

Hen egg white Lyz, bovine milk β-Lac, and human α-Syn amyloid fibril samples (all 120 μM monomer equivalent concentration) were stirred for up to 15 days. Samples were taken out periodically, deposited on mica, and imaged using AFM. Typical AFM images representing 10 × 10 μm surface areas are shown together with 4× magnified insets. Scale bars, 2 μm.

Qualitative inspection of the AFM images throughout the experiment (Figure 3) showed that the amyloid fibrils were fragmented into much smaller particles under the applied mechanical perturbation (Figures 2 and 3) as expected. However, the rate of division and shortening of the particles' lengths was seen to differ between the three different fibril types analyzed (Figures 3 and S2). Analysis of the time evolution of the fibril height and length distributions obtained by quantification of individual particles in the AFM images over the course of the experiment confirmed that fibril fragmentation did not cause detectable changes in fibril morphology and fibril width through lateral association and dissociation. Average fibril heights in the AFM images, indicative of fibril widths, remained consistent throughout the experiment for Lyz and α-Syn. The same was also largely observed for β-Lac, with the exception that a small second population of taller polymers at the very end of the fragmentation time course after 432,000 s was observed (height graphs in Figures 3 and S2). Hence the division of the fibrils under mechanical perturbation applied has resulted in a shortening of average fibril length.

To confirm that the changes in fibril length by fibril division did not cause disaggregation or release of monomer/small oligomers (e.g., dimers), we next determined the residual monomer concentration of the samples. For each fibril type, aggregates were pelleted by centrifugation (75k rpm, 15 min) after fragmentation time course and the presence of monomer in the supernatants was quantified by SDS-PAGE. The comparison between the initial samples and those fragmented over 2 weeks showed no substantial changes in the protein composition of the supernatants, with differences of less than 2% for all amyloid systems analyzed (Lyz: 1.4%, β-Lac: <1%, and α-Syn: 1.3%, Figure S3). These data confirmed that the time-dependent imaging experiments we carried out pertain almost exclusively to the fibril division processes along the length of the pre-formed fibrils and therefore contain valuable information on their division rates and their stability to division.

Time Evolution of Fibril Length Distributions Converges to Time-Independent, Characteristic, Self-Similar Length Distribution Shapes

The fibril samples formed from different protein precursors have different initial length distributions (as seen in Figures 2 and 3). However, fibril division is itself a strongly length-dependent process (Xue and

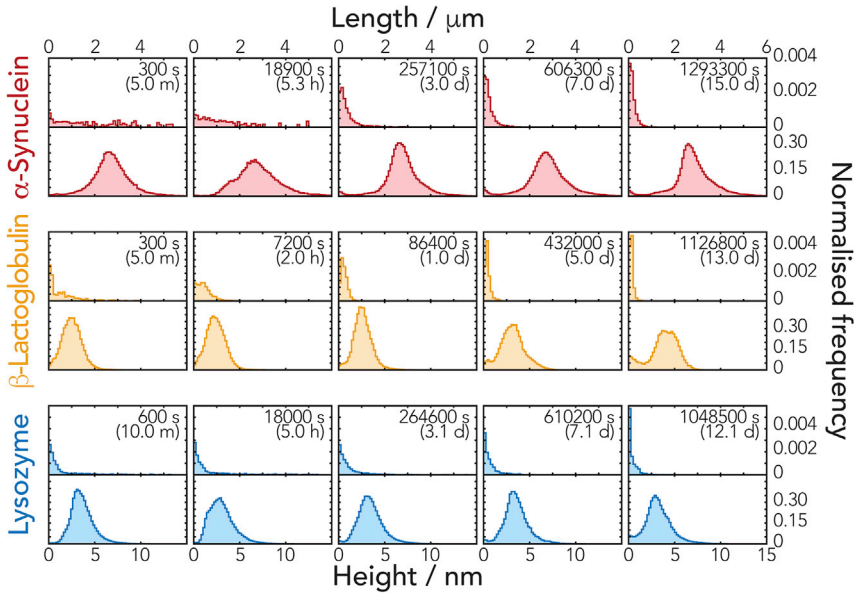

Figure 3. Fibril Length and Height Distributions Extracted from AFM Images of the Fibrils Undergoing Fragmentation by Mechanical Perturbation

Normalized length (upper row of each sample) and height (lower row of each sample) distributions of fibril particles corresponding to the same AFM images in Figure 2 are shown as histograms. The histograms are shown using the same length and height scales, respectively, for comparison.

Radford, 2013) as short fibril particles will be more resistant to division compared with longer particles, irrespective of any differences in the intrinsic stability of the different fibril types to division. Therefore, to compare the stability of amyloid fibrils with different suprastructures and length distributions toward division, a new approach to extract information intrinsic to each fibril type independent of their experimentally different initial length distributions must be developed. Consequently, in parallel with the experiments described earlier in the article, we mathematically analyzed the division equation of amyloid fibrils so that key information on the stability of amyloid fibrils to division could be resolved. We first describe the division of amyloid fibrils mathematically using a continuous framework based on the partial differential equation (PDE) Equation 1. As the number of monomers inside a fibril observed in the image data is large, typically in the order of 10^2 or more, we assumed continuous variables x and y that correspond to the length of fibrils (for example, as defined in Figure 1B where y is the length of the parent fibril and x is the length of one of the daughter fibrils). This approach has the advantage that the infinite set of ordinary differential equations (ODEs) normally used to describe the length-dependent division processes (e.g., Knowles et al., 2009; Xue et al., 2008; Xue and Radford, 2013) can now be collapsed into a single continuous PDE that can be treated analytically (see Supplemental Information for details). Denoting $u(t, x)$ as the distribution of fibrils of length x at time t in number concentration units (e.g., molar units), Equation 1 is the mathematical translation of the pure division model described by the schematics in Figures 1B–1D, where we assume that any parent fibril can divide into two daughters and the end-to-end reattachment rate of daughter fibrils is negligible (Hill, 1983):

$$\frac{\partial}{\partial t}u(t,\,x) = \; -\alpha_0(\alpha x)^{\gamma}u(t,\,x) + 2\int_{y=x}^{\infty}\frac{1}{y}\kappa_0\left(\frac{x}{y}\right)\alpha_0(\alpha x)^{\gamma}u(t,\,y)dy \qquad \text{(Equation 1)}$$

In Equation 1, $\partial u(t, x)/\partial t$ denotes the time (t) evolution of the concentration of fibrils with length x. Here, we model the total division rate constant of fibrils of size x using the power law $\alpha_0(\alpha x)^{\gamma}$ (Hill, 1983), which we denote as $B(x)$ (see Supplemental Information), where α_0 is a constant unit reference we set to 1 s^{-1}. The first term in Equation 1 therefore, denotes the rate of loss of fibrils with length x by division into smaller fibrils. The probability that after dividing, a given parent fibril of length y gives rise to daughter fibril fragments of length x and y-x depends on the ratio of the lengths (x/y) (Xue and Radford, 2013) and is given by the probability density function $(1/y)\kappa_0(x/y)$. The second integral term in Equation 1, therefore, denotes the total gain of fibrils with length x by division of all fibrils with length y that are larger than x. Interestingly,

Equation 1 describes a fundamental division process that is mathematically analogous to the division of molecules, macroscopic materials, and cells (Escobedo et al., 2005; Robert et al., 2014), and we have mathematically proved that its behavior is entirely and uniquely dictated by three properties: α that describes the magnitude of the division rate constant, γ that describes the fibril length dependence of the division rate constant, and κ_0 that describes the probability of division at any given position along a fibril, also called the fragmentation kernel (Doumic et al., 2018). We then proceeded to solve Equation 1 analytically with regard to α, γ, and κ_0 using theoretical results shown in Escobedo et al. (2005) and Doumic et al. (2018) (see Supplemental Information). From our solution, we note four key predictive insights that emerged from our analysis (Figure 4).

First, we note that given enough time, the decay of the average fibril length will converge to the same rate independently of the initial fibril length distributions. This result comes from that after a sufficiently long time, the reduction of average length of the fibril length distribution can be described as a power law versus time (Equation 2, see Supplemental Information):

$$\mu(t) = C \cdot t^{-1/\gamma} \quad \text{(Equation 2)}$$

where C is a constant. As seen in Equation 2, the experimentally observable average length of a sample, $\mu(t)$, is predicted to tend toward a straight line when plotted on a log-log plot with the slope of the line representing $-1/\gamma$ (Equation 2, black line in Figure 4B) because the long-time behavior of Equation 1 can be described as a power law.

Second, we note that given enough time, the fibril length distribution will converge to the same shape independently of the initial state of the fibril length distribution. After a sufficiently long time ($t \gg t_0$), the distribution of fibril lengths tends toward a time-independent distribution shape, $g(x_g)$, that scales only with t and γ, but does not depend on the initial length distribution (Equation 3 and Supplemental Information).

$$g(x_g) \approx f(t,x) \cdot t^{-\frac{1}{\gamma}}, \quad x_g = x t^{\frac{1}{\gamma}}, \quad \textit{For any } t \gg t_0 \quad \text{(Equation 3)}$$

where $f(t, x)$ are experimentally measured length distributions. This point is of key importance for characterizing and predicting fibril division processes because it establishes that for any fibril type under certain conditions (1) a distinct fibril length distribution shape (Figure 4A) will be reached independently of the initial fibril length distribution and (2) the length distribution and the average length will shrink as function of time in a predictive manner as fibrils continue to divide (e.g., the black line in Figure 4B for the mean length) but the shape of the distribution will not change as function of time, i.e., the length distribution can be rescaled to the same $g(x_g)$ using Equation 3 at any time t along the black line in Figure 4B if t is sufficiently large. We refer to the distributions with the scaling property and shape invariance property as "self-similar length distributions" (Figure 4A).

The existence of a self-similar length distribution that is initial length distribution independent and shape invariant over time, as well as the predictable decay of fibril lengths as fibrils divide (e.g., the reduction of the average length in Figure 4B) can be seen as a characteristic behavior specific to individual fibril types under distinct conditions. This fibril division behavior can, therefore, be classed as a type of intrinsic dynamic stability of the fibrils. One way to visualize this property is shown in Figure 4B represented by the black line, here referred to as the fibril type's "asymptotic line" under the conditions applied. Any fibril population above this line is relatively unstable and will rapidly divide, pushing the average length toward the line (red- and yellow-colored near-vertical arrows showing rapid decay of unstable fibril lengths). In contrast, any fibril population below this line is comparatively stable or metastable and will only slowly evolve toward the line through division (green- to blue-colored near-horizontal arrows showing slow decay of stable fibril lengths toward the black line). Importantly, this result also indicates that the dynamic stability of fibrils to division represented by the asymptotic line (1) can be determined from experimental data, (2) is intrinsic to fibril type and conditions applied, and (3) can be compared independently of varied starting fibril length distributions, if the characteristic self-similar length distributions that contain information about the intrinsic dynamic stability of the fibrils is reached (e.g., the asymptotic line is reached in an experiment running for sufficiently long length of time).

Third, we note that the probability of division at the center of a fibril when compared with the shedding of small particles from fibril edge can be evaluated from the experiments. The self-similar length distributions contain information about κ_0. Figure 4C shows how different self-similar fibril length distributions are indicative of

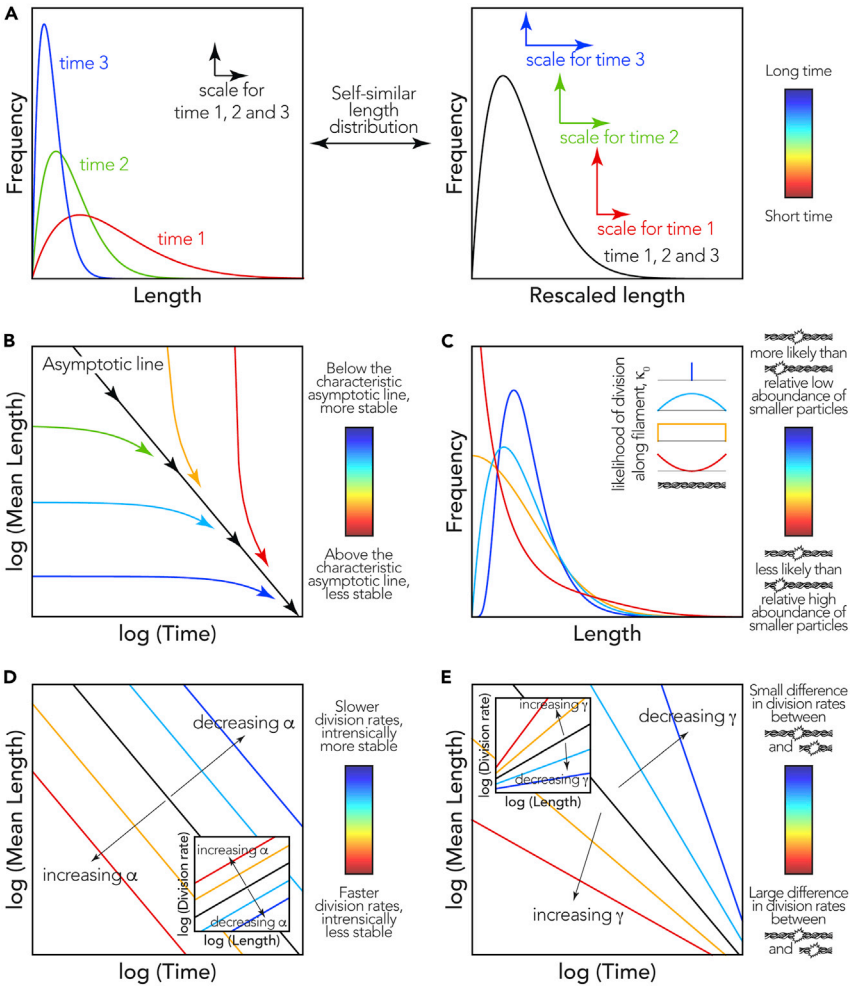

Figure 4. Illustration of The Key Insights Emerging from the Mathematical Analysis of the Division Model

The behavior of the division equation Equation 1 is entirely and uniquely dictated by a set of three properties: α, γ, and κ_0. Several key predictive insights emerged from the analytical solution of Equation 1 with regard to these three properties.

(A) The three example length distributions in the left panel can be rescaled to show the same distribution shape in the right panel, illustrating the concept of self-similar length distributions.

(B) After a period of time, the self-similar length distribution shape is reached. From this point, the reduction in the average length of the fibril length distribution can be described as a power law versus time. The decay of mean length of a sample is predicted to tend toward a straight line, the asymptotic line, when plotted on a log-log plot with the slope of the line representing $-1/\gamma$ (black line in B, D, and E). The asymptotic line denoting mean fibril lengths decay also does not depend on the initial length distribution (colored lines in B).

(C) The self-similar length distribution shape contains information about κ_0, which describes how likely a fibril will divide in the middle versus shedding a small fragment from the edge. A κ_0 indicative of fibril types that are more likely to divide in the middle will result in fibril length distributions with a distinct peak and low relative population of small fragments (dark blue and light blue curves). In contrast, κ_0 indicative of fibril types and conditions that promote equal likelihood of division along the fibril or even favor shedding of small fragments from fibril edges will result in self-similar fibril length distributions that have a larger relative population of small fibril fragments (orange and red curves) compared with κ_0 values favoring division in the center of the fibrils.

(D and E) (D) and (E) illustrate how the black asymptotic line describing the decay of fibril lengths in (A) is dictated by the parameters α and γ, respectively. For each panel, the color bar to the right illustrates the different properties associated with the colors in the panel (e.g., division in the center versus at the edge of a fibril for (C), and division of a long versus a short fibril in (E)).

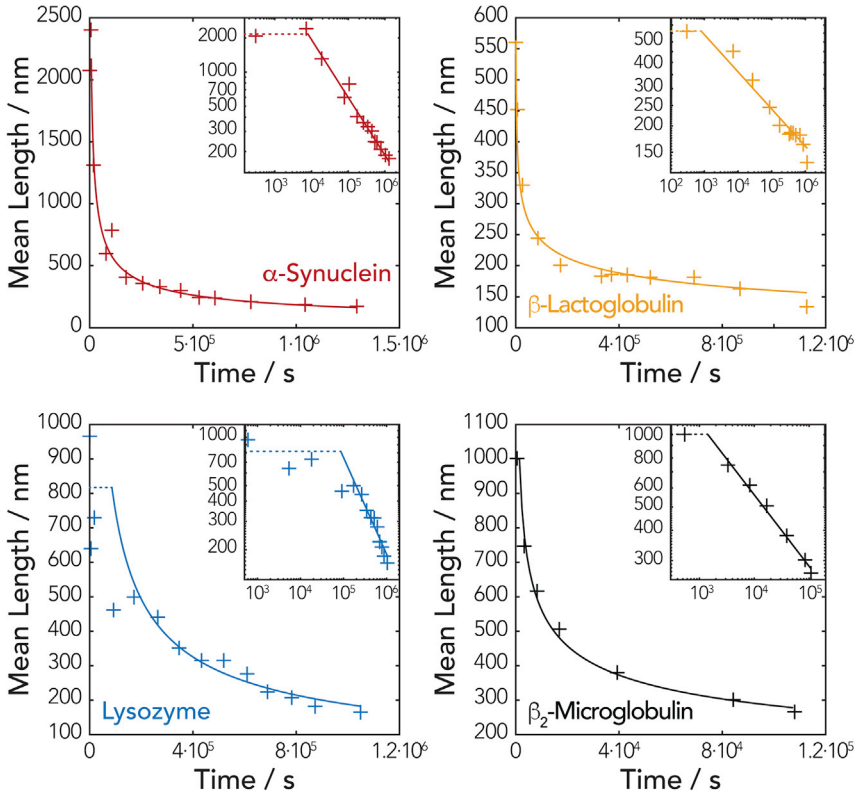

Figure 5. Fitting the Fibril Division Model to Fibril Length Decay Data Extracted from AFM Images

The analytical solution of our division model shows the decay of average length as function of the γ parameter in Equations 2 and S22. Equation S22 was fitted to the decay of average fibril length during division for each of the fibril types analyzed (including previously published data for β_2m fragmentation under the same mechanical perturbation conditions in Xue and Radford (2013). The solid fitted lines represent the time regimen where the length distributions closely approached the asymptotic line and the self-similar distribution shape where Equation 2 is valid (Transparent Methods).

different κ_0 probability functions. As seen in Figure 4C, a κ_0 indicative of fibril types that are more likely to divide in the middle will result in fibril length distributions with a distinct peak and low relative population of small fragments. In contrast, a κ_0 indicative of fibril types and conditions that promote equal likelihood of division along the fibril or even favoring the shedding of fragments from fibril edges will result in self-similar fibril length distributions that have large relative population of small fibril fragments that may possess enhanced cytotoxic and/or infective potential compared with κ_0 favoring division in the center of the fibrils.

Finally, the dynamic stability of fibrils to division, their propensity to break at different lengths, can be determined. The first-order division rate constant $B(x) = \alpha_0(\alpha x)^{\gamma}$ that describes the division of the fibrils as a function of their length x can be directly evaluated from the self-similar length distribution and γ (see Equation 2) when $t >> t_0$ (see Supplemental Information and Equation S21) where t_0 is the start of the experiment. Thus, the division rate constant $B(x)$ can be determined by experimentally observing how fibril length distributions change with time when the self-similar fibril length distribution is obtained, and they are important parameters for defining and comparing the fibrils' intrinsic dynamic stability to division. The effect of different values of α and γ on fibril stability is visualized in Figures 4D and 4E as characteristic of the asymptotic line plotted in log-log plots of average length versus time. The enumeration of the asymptotic line described by $B(x)$ will subsequently enable direct quantitative comparison of the fibrils' stabilities toward division.

The Division Properties of Amyloid Fibrils Can Be Obtained from Image Data, and Their Complex Stability to Division Can Be Compared

Applying the results of the mathematical analysis to the experimental AFM image datasets, the parameters γ, α, and the characteristic self-similar length-distributions $g(x_g)$ indicative of κ_0 can be extracted and

Sample	$\gamma \pm SE$	α/nm^{-1} (log $\alpha \pm SE$)	B (100 nm)/s^{-1} (log $B \pm SE$)	Height (Fibril Width)/nm
α-Syn	2.0 ± 0.3	2.6×10^{-6} (−5.6 ± 0.2)	9.2×10^{-8} (−7.0 ± 0.3)	6.8 ± 0.6
β-Lac	5.7 ± 0.8	1.8×10^{-4} (−3.7 ± 0.2)	1.2×10^{-10} (−9.9 ± 0.8)	3.0 ± 0.5
Lyz	1.7 ± 1.0	9.4×10^{-7} (−6.0 ± 0.9)	2.0×10^{-7} (−6.7 ± 1.0)	3.1 ± 0.4
β_2m[a]	3.4 ± 0.4	5.6×10^{-5} (−4.3 ± 0.3)	2.5×10^{-8} (−7.6 ± 0.4)	5.4 ± 0.6

Table 1. Parameters from the Division Analysis of the Different Fibril Types
[a]Reanalysis of data from Xue and Radford (2013).

meaningfully compared as a measure of the fibrils' intrinsic stability to division. We first determined the γ values for each of the fibril types, by globally fitting a variant of Equation 2 to the time evolution of average fibril length (see Transparent Methods, Figure 5). We also reanalyzed previously published dataset on β_2m fibril fragmentation under the same mechanical perturbation conditions (Xue and Radford, 2013) using our new aforementioned theoretical results and included the reanalysis in the comparison.

The constant γ was determined from least-squares fitting of our analytical result to the data (Transparent Methods). The power law relationship (Equation 2) parameterized with γ determined by global analysis was visualized on a log-log plot of mean fibril length versus time in Figure 5, together with the measured mean fibril lengths. The resulting γ values are listed in Table 1. A γ value of 1 would suggest that the division rate of fibrils is only dependent on the number of division sites per fibril, which is linearly related to the number of monomers in the fibrils and in turn to the length of the fibrils. However, the γ values for α-Syn, β-Lac, and β_2m are all significantly larger than 1, indicating highly length-dependent microscopic division rates for division sites in these fibril types. Of the four fibril types analyzed, the division of Lyz fibrils yielded a γ value closest to 1. This suggests that the division rates for Lyz fibrils may only depend on the number of available division sites along the fibrils. β-Lac fibrils yielded the highest γ value of the fibril types analyzed. This demonstrates that β-Lac fibril fragmentation is highly length dependent, and small β-Lac fibril fragments are more resistant to further fragmentation compared with the other fibril types. This behavior may corroborate with an increased lateral association of small β-Lac fibril fragmentation fragments observed on the height distributions at the end of the time course experiments (height graphs in Figure 3 and S2). As seen in Figure 5, the later time points for all our fibril types follow a straight line on the log-log plots (solid section of the fitted lines in Figure 5), indicating that the self-similar length distributions, and hence the asymptotic line, were sufficiently reached in all cases. The analysis also revealed that all the fibril types analyzed approached the self-similar length distribution shapes in less than 5 h, with the exception of the Lyz samples that reached the self-similar distribution in approximately 24 h.

The α values were subsequently calculated (listed in Table 1) with Equation S21 using all the fibril length distributions at time points post reaching the near-characteristic self-similar distribution shapes (represented by the solid lines in Figure 5). Once both α and γ values have been extracted from the length distribution data, the division rate constant $B(x)$ can be obtained for fibrils of any length x. Table 1 shows the division rate constant calculated for fibrils of 100 nm. The asymptotic line for the fibrils types characterized by the division rate constant $B(x)$ (Figure 6B) or by fibril mean length (Figure 6A) as a function of time was also visualized and compared independently of initial fibril length, showing that α-Syn and Lyz fibrils fragment the fastest at long times under the mechanical perturbation applied, suggesting that these fibrils were less stable than the β-Lac and β_2m fibrils.

Next, we determined the shape of the self-similar length distributions for each fibril type by rescaling the experimental length distributions to $g(x_g)$ with Equation 3 using the γ values obtained earlier. As with the evaluation of α values, only time points where the length distributions closely approached the self-similar length distribution (time points in the section represented by the solid lines in Figure 5) were averaged to obtain $g(x_g)$ for each fibril type (Figure S4). Figure 6C shows how the self-similar length distribution shapes compare with each other at extended times (2 weeks) when calculated using $g(x_g)$ (Figure S4) with Equation 3. As seen in Figure 6C, Lyz fibrils tend to produce high relative populations of small particles less than 100 nm long followed by α-Syn and then β_2m. On the other hand, the division of β-Lac fibrils resulted in a lower relative population of small particles over the same long timescale used for the other fibril types.

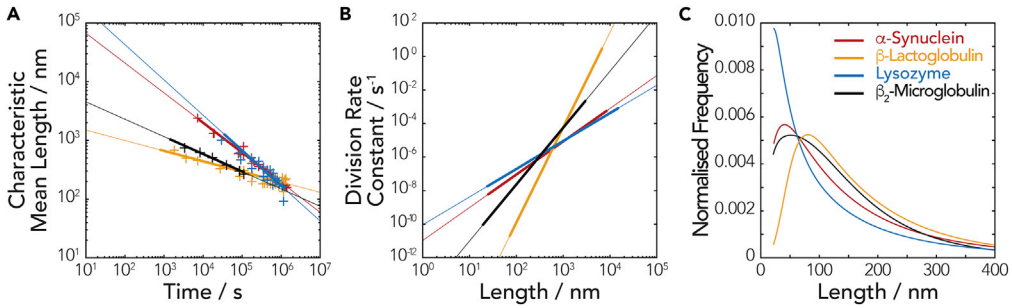

Figure 6. Comparing the Stability toward Division Of Different Amyloid Fibril Types

(A–C) The decay of mean lengths (A), the division rate constants as function of fibril length (B), and the self-similar length distribution shapes (C) for hen egg Lyz (blue), bovine milk β-Lac (yellow), human α-Syn (red), and human β_2m (black; data from Xue and Radford, 2013) amyloid fibril samples undergoing division by fibril fragmentation under mechanical perturbation. All curves were calculated using α, γ, and $g(x_g)$ obtained from our analysis of the experimental AFM images. In (A), the thicker portion of the lines denote the time range where the characteristic self-similar length distribution shape is observed in the imaging experiments (i.e., corresponding to the time regime represented by the solid fitted lines in Figure 5), and crosses are the experimental data points that have closely reached the self-similar distribution shapes shown in the same plot. In (B), the thicker portion of the lines denotes the range of fibril lengths observed experimentally on the AFM images. In (C), the distributions were calculated using self-similar distributions $g(x_g)$ in Figure S3 after 2 weeks.

Finally, to validate our model and the predictive power of our approach, we performed direct simulations of the fibril division time course (Figure 7) using only the individual sets of division parameters obtained for each of our fibril types. For each simulation, we used the initial experimental length distributions (dashed lines in Figure 7) directly as the starting points for the simulations. The large set of ordinary differential equations describing the chemical master equation for the system (Xue and Radford, 2013) was then solved to see whether our analytical model was able to predict the full division behavior and the time evolution of the fibril length distributions for each fibril type. As seen in Figure 7, the result of the numerical simulations based on our results show remarkable agreement with the experimental data. This unequivocal result validated the fact that the set of three properties γ, α, and κ_0 are indeed capable of fully and uniquely describing the complex amyloid division processes, and the enumeration of these properties yield valuable insights. Such insights allow meaningful comparison of the amyloid fibrils' intrinsic stability to division.

DISCUSSION

The understanding of the properties that underline the biological activities of amyloid nanostructures, such as their cytotoxic and infectious potentials, is crucial for understanding why some amyloids are associated with devastating human diseases. The division of amyloid fibrils, for example, through fibril fragmentation by mechanical perturbation (Xue et al., 2008; Xue and Radford, 2013), enzymatic action (Chernoff et al., 1995; Glover and Lindquist, 1998), or other cellular or environmental perturbations, is a key step in their life cycle that results in the exponential growth in the number of amyloid particles. Simultaneously, daughter particles resulting from the division of parent fibrils cause a reduction in the overall size distribution as division proceeds. These two consequences of division are undoubtedly linked to the enhancement of the cytotoxic and infectious potentials of disease-associated amyloid (Marchante et al., 2017; Xue et al., 2009a). The amyloid fibrils' resistance to division, i.e., the stability of the amyloid fibrils to division, rationalizes these two fundamental requirements for pathogenicity associated with amyloid. Akin to uncontrolled division of cells or any pathogenic microorganisms, the division step in the amyloid life cycle (Figure 1) could be a key determinant in their overall potential to be associated with properties in the amyloid and prion-associated pathology.

Here, we have developed a theory, as well as an experimental approach utilizing our theoretical insights, to resolve the amyloid fibrils' dynamic stability to division. These represent a step forward in how we are able to study the amyloid fibril division processes such as in fibril fragmentation and prion propagation, essentially the replication step in the amyloid life cycle. It also allows the direct comparison between amyloid particles of different molecular types and quantifies the difference in division and stability between those that are and are not disease associated. Specifically, we have applied our theoretical results to the comparison of a diverse set of amyloid assemblies consisting of human α-Syn (a neurodegenerative

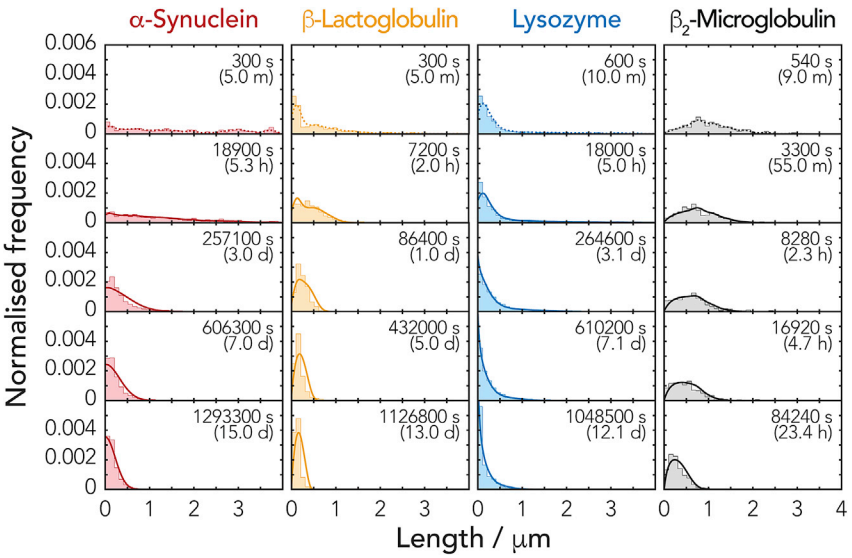

Figure 7. Validation of the Division Parameters α, γ, and κ_0 and Their Predictive Power

Full direct simulation of fibril fragmentation processes was carried out using α, γ, and κ_0 determined from the image data. For each fibril type, the initial normalized frequency distribution (dashed lines in top row) was used directly as the initial state for the simulations. The resulting simulated evolution of length distributions solely based on the calculated α and γ values and estimated shapes κ_0 (see Methods) are compared with the experimental data shown as histograms.

disease-associated amyloid, sample formed under physiological solution conditions), human β_2m (a systemic amyloidosis disease-associated amyloid, sample formed under acidic pH, data from Xue and Radford, 2013), bovine β-Lac, and hen egg white Lyz (later two cases are both biophysical model systems not directly related to human disease but converted to amyloid when subjected to heating in acidic pH). By fully analyzing and comparing their division behavior, which is uniquely described by the triplet of parameters (α, magnitude of the division rate constant; γ, fibril length dependence of the division rate constant; and κ_0, probability of division at any given position along a fibril) under identical mechanical perturbation for long timescales using our approach, we show a remarkable difference in the stability of these different amyloid assemblies relative to each other and how they divide (summarized in Figure 8). Interestingly, for the four fibril types we included here, considering the division rate constant B with their cross-sectional area, the disease-associated human α-Syn fibrils demonstrate the lowest overall stability to division followed by Lyz, human β_2m, and finally β-Lac particles, which are the most stable toward division (Figure 8 last row). Based on the comparison of the α and γ parameters that together describe the division rates $B(x)$, the likelihood that small α-Syn particles (<100 nm long) will divide is similar to that of Lyz particles of identical length despite having more than double the mean width (and thus around four times bigger cross-sectional area, Table 1 and Figure 8). More importantly, the division of α-Syn particles also results in a larger relative concentration of small particles compared with β_2m and β-Lac. These results show that human α-Syn amyloid fibrils are relatively unstable assemblies capable of a more rapid shedding of small particles that could well possess enhanced cytotoxic and infectious potentials (Peelaerts et al., 2015) through division compared with the other fibril types investigated here. Thus, our results also directly suggest a testable causality link between the low stability of α-Syn fibrils to division and recent observations that human α-Syn may behave in a prion-like manner in cell-to-cell propagation and their cytotoxicity (Steiner et al., 2018).

As the division of amyloid fibrils is an integral part in the propagation of the amyloid conformation (Figure 1), the nanoscale material properties of amyloid underpin processes that drive the proliferation of amyloid, as well as their varied roles in biology. Therefore, it is important to appreciate the suprastructural properties of amyloid (e.g., clustering, bundling, twist, stiffness, width distribution, orientation distribution, and length distribution, etc.) at mesoscopic (nanometre to micrometre) length scales, as these properties will influence how individual amyloid fibrils divide. Our data show that despite all amyloid consisting of a cross-beta core structure, their ability to resist division through fragmentation promoted by mechanical perturbation varies strongly between fibril types. As the stability of amyloid fibrils to division will depend on their suprastructural properties, which in turn depend on their precise structure at atomic level,

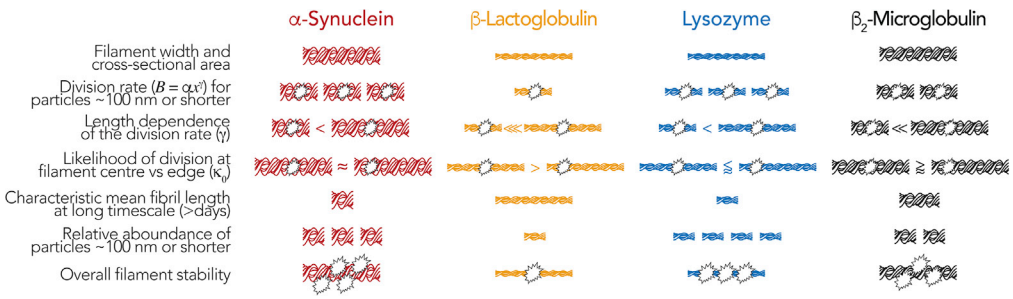

Figure 8. Schematic Summary of the Fibril Division Properties and Their Consequences Compared between Each of the Fibril Types

Comparison of the fibril division profiles reveals differences in the dynamical stability toward breakage for the four different types of amyloid fibrils and suggests that disease-related amyloid has lowered stability toward breakage and increased likelihood of shedding smaller particles compared with amyloid not related to disease. In the illustrations, the fibril width, number, and number of breakage symbols are not to scale and denote the relative rankings for the different properties.

mesoscopic-level structural properties may well be the missing link between amyloid structure and the varied biological effects and consequences that different amyloid types evoke under different conditions. Although the results reported here reveal the breakage behavior of fibril populations, future advances in AFM imaging may allow either individual polymorphs in a fibril population to be distinguished or individual fibrils to be tracked in real time, further revealing how fibrils divide as individuals. Thus, it should be possible to generate a structure-activity relationship correlating the suprastrucutral properties of amyloid, their ability to divide, and their cytotoxic and/or infectious potentials. Understanding this structure-activity relationship for amyloid assemblies could lead to the design of bio-safe polymers with tuned mechanical and nanomaterials properties as well as rationalize the disease-associated properties of amyloid structures.

Analogous to the diverse response of soluble folded proteins toward unfolding by chemical denaturants, thermal melting, mechanical force, etc., the stability of amyloid fibrils could also vary depending on the nature of the perturbation. Indeed, amyloid fibrils may break down in the presence of chemical, thermal, or enzymatic action (Baldwin et al., 2011; Chernoff et al., 1995; Glover and Lindquist, 1998; Knowles et al., 2007; Shammas et al., 2011; Surmacz-Chwedoruk et al., 2014), and their relative resistance or stability to different stresses, including those associated with physiological changes involved in human disorders, is not known. In particular, understanding how enzymatic action by molecular chaperones such as Hsp104 or ClpB promotes amyloid division, degradation, and/or propagation of amyloid conformation (Chernova et al., 2017; Scior et al., 2016) in relevant cases may be key in resolving the complex behavior of the amyloid life cycle in a biological context. In summary, the combined theoretical and experimental work we report here will enable the characterization and comparison of the amyloid division processes and the relative stabilities of amyloid assemblies. Both properties are fundamental in understanding the life cycle of disease-associated amyloid as well as the normal roles of functional amyloid in biology.

Limitations of the Study

The division model (assumptions illustrated in Figure 1) does not take into account the possibilities that newly created fibril ends by division may be more dynamic, disordered, and/or be "sticky ends" in their interactions with other fibril ends or surfaces compared with established fibril ends for elongation. The results reported here reveal the overall breakage behavior of the fibril populations, as our experiments may contain a mixture of similar but, nevertheless, different polymorphs that could not be readily distinguished in our images. Future advances in AFM imaging allowing either individual polymorphs in a fibril population to be distinguished or individual fibrils to be tracked in real time will resolve breakage behavior of individual fibril polymorphs. The model assumptions and limitations may also leave scope for improvements in the model to be pursued in future work by the field.

Resource Availability

Lead Contact

Wei-Feng Xue (w.f.xue@kent.ac.uk).

Materials Availability

This study did not generate new unique reagents.

Data and Code Availability

The published article includes all datasets generated and analyzed during this study. The list of all (over 220,000) raw fibril lengths and associated analysis code supporting the current study is available from the corresponding author on request.

METHODS

All methods can be found in the accompanying Transparent Methods supplemental file.

SUPPLEMENTAL INFORMATION

Supplemental Information can be found online at https://doi.org/10.1016/j.isci.2020.101512.

ACKNOWLEDGMENTS

We thank the members of the Xue group and the Kent Fungal Group for helpful comments throughout the preparation of this manuscript, and Ian Brown for technical support. We also thank Sheena Radford for insightful discussions, as well as help and support on the reanalysis of β_2-microglobuling fragmentation dataset. This work was supported by funding from INRIA (W.-F.X. and M.D.), the European Research Council (ERC) Starting Grant number 306321, SKIPPERAD (M.D.) the Biotechnology and Biological Sciences Research Council (BBSRC) UK grants BB/J008001/1 (W.-F.X.) as well as BB/F016719/1 (D.M.B.), and the Wellcome Trust grant 209171/Z/17/Z (D.M.B.).

AUTHOR CONTRIBUTIONS

D.M.B. designed the research, conducted the experiments, and analyzed the data. M.T. designed the research, developed the theory, wrote the analytical software tools, and analyzed the data. R.M. and T.J.P. conducted the experiments. D.P.S. provided reagents and methods and analyzed the data. M.F.T. designed the research and analyzed the data. M.D. designed the research, developed the theory, and analyzed the data. W.-F.X. designed the research, wrote the analytical software tools, developed the theory, analyzed the data, and managed the research. The manuscript was written through contributions of all authors.

DECLARATION OF INTERESTS

The authors declare no conflicts of interest.

Received: March 16, 2020
Revised: July 31, 2020
Accepted: August 26, 2020
Published: September 25, 2020

REFERENCES

Aguzzi, A., Heikenwalder, M., and Polymenidou, M. (2007). Insights into prion strains and neurotoxicity. Nat. Rev. Mol. Cell Biol. *8*, 552–561.

Ankarcrona, M., Winblad, B., Monteiro, C., Fearns, C., Powers, E.T., Johansson, J., Westermark, G.T., Presto, J., Ericzon, B.G., and Kelly, J.W. (2016). Current and future treatment of amyloid diseases. J. Intern. Med. *280*, 177–202.

Baldwin, A.J., Knowles, T.P., Tartaglia, G.G., Fitzpatrick, A.W., Devlin, G.L., Shammas, S.L., Waudby, C.A., Mossuto, M.F., Meehan, S., Gras, S.L., et al. (2011). Metastability of native proteins and the phenomenon of amyloid formation. J. Am. Chem. Soc. *133*, 14160–14163.

Barritt, J.D., Younan, N.D., and Viles, J.H. (2017). N-terminally truncated amyloid-beta(11-40/42) cofibrillizes with its full-length counterpart: implications for alzheimer's disease. Angew. Chem. Int. Ed. *56*, 9816–9819.

Berson, J.F., Theos, A.C., Harper, D.C., Tenza, D., Raposo, G., and Marks, M.S. (2003). Proprotein convertase cleavage liberates a fibrillogenic fragment of a resident glycoprotein to initiate melanosome biogenesis. J. Cell Biol. *161*, 521–533.

Bleem, A., and Daggett, V. (2017). Structural and functional diversity among amyloid proteins: agents of disease, building blocks of biology, and implications for molecular engineering. Biotechnol. Bioeng. *114*, 7–20.

Breydo, L., and Uversky, V.N. (2015). Structural, morphological, and functional diversity of amyloid oligomers. FEBS Lett. *589*, 2640–2648.

Brundin, P., and Melki, R. (2017). Prying into the prion hypothesis for Parkinson's disease. J. Neurosci. *37*, 9808–9818.

Buell, A.K., Galvagnion, C., Gaspar, R., Sparr, E., Vendruscolo, M., Knowles, T.P., Linse, S., and Dobson, C.M. (2014). Solution conditions determine the relative importance of nucleation and growth processes in alpha-synuclein aggregation. Proc. Natl. Acad. Sci. U S A *111*, 7671–7676.

Cappai, R., Leck, S.L., Tew, D.J., Williamson, N.A., Smith, D.P., Galatis, D., Sharples, R.A., Curtain,

C.C., Ali, F.E., Cherny, R.A., et al. (2005). Dopamine promotes alpha-synuclein aggregation into SDS-resistant soluble oligomers via a distinct folding pathway. FASEB J. *19*, 1377–1379.

Chapman, M.R., Robinson, L.S., Pinkner, J.S., Roth, R., Heuser, J., Hammar, M., Normark, S., and Hultgren, S.J. (2002). Role of Escherichia coli curli operons in directing amyloid fiber formation. Science *295*, 851–855.

Chernoff, Y.O., Lindquist, S.L., Ono, B., Inge-Vechtomov, S.G., and Liebman, S.W. (1995). Role of the chaperone protein Hsp104 in propagation of the yeast prion-like factor [psi+]. Science *268*, 880–884.

Chernova, T.A., Wilkinson, K.D., and Chernoff, Y.O. (2017). Prions, chaperones, and proteostasis in yeast. Cold Spring Harb. Perspect. Biol. *9*, a023663.

Cox, B., Ness, F., and Tuite, M. (2003). Analysis of the generation and segregation of propagons: entities that propagate the [PSI+] prion in yeast. Genetics *165*, 23–33.

Derdowski, A., Sindi, S.S., Klaips, C.L., DiSalvo, S., and Serio, T.R. (2010). A size threshold limits prion transmission and establishes phenotypic diversity. Science *330*, 680–683.

Dobson, C.M. (1999). Protein misfolding, evolution and disease. Trends Biochem. Sci. *24*, 329–332.

Doumic, M., Escobedo, M., and Tournus, M. (2018). Estimating the division rate and kernel in the fragmentation equation. Ann. Henri Poincare *35*, 1847–1884.

Escobedo, M., Mischler, S., and Ricard, M.R. (2005). On self-similarity and stationary problem for fragmentation and coagulation models. Ann. Henri Poincare *22*, 99–125.

Glover, J.R., and Lindquist, S. (1998). Hsp104, Hsp70, and Hsp40: a novel chaperone system that rescues previously aggregated proteins. Cell *94*, 73–82.

Hill, T.L. (1983). Length dependence of rate constants for end-to-end association and dissociation of equilibrium linear aggregates. Biophys. J. *44*, 285–288.

Hu, B., Shen, Y., Adamcik, J., Fischer, P., Schneider, M., Loessner, M.J., and Mezzenga, R. (2018). Polyphenol-binding amyloid fibrils self-assemble into reversible hydrogels with antibacterial activity. ACS Nano *12*, 3385–3396.

Hu, X., Crick, S.L., Bu, G., Frieden, C., Pappu, R.V., and Lee, J.M. (2009). Amyloid seeds formed by cellular uptake, concentration, and aggregation of the amyloid-beta peptide. Proc. Natl. Acad. Sci. U S A *106*, 20324–20329.

Jakhria, T., Hellewell, A.L., Porter, M.Y., Jackson, M.P., Tipping, K.W., Xue, W.F., Radford, S.E., and Hewitt, E.W. (2014). beta2-microglobulin amyloid fibrils are nanoparticles that disrupt lysosomal membrane protein trafficking and inhibit protein degradation by lysosomes. J. Biol. Chem. *289*, 35781–35794.

Khan, T., Kandola, T.S., Wu, J., Venkatesan, S., Ketter, E., Lange, J.J., Rodriguez Gama, A., Box, A., Unruh, J.R., Cook, M., et al. (2018). Quantifying nucleation in vivo reveals the physical basis of prion-like phase behavior. Mol. Cell *71*, 155–168 e157.

Knowles, T.P., and Buehler, M.J. (2011). Nanomechanics of functional and pathological amyloid materials. Nat. Nanotechnol. *6*, 469–479.

Knowles, T.P., Fitzpatrick, A.W., Meehan, S., Mott, H.R., Vendruscolo, M., Dobson, C.M., and Welland, M.E. (2007). Role of intermolecular forces in defining material properties of protein nanofibrils. Science *318*, 1900–1903.

Knowles, T.P., Vendruscolo, M., and Dobson, C.M. (2014). The amyloid state and its association with protein misfolding diseases. Nat. Rev. Mol. Cell Biol. *15*, 384–396.

Knowles, T.P., Waudby, C.A., Devlin, G.L., Cohen, S.I., Aguzzi, A., Vendruscolo, M., Terentjev, E.M., Welland, M.E., and Dobson, C.M. (2009). An analytical solution to the kinetics of breakable filament assembly. Science *326*, 1533–1537.

Lara, C., Usov, I., Adamcik, J., and Mezzenga, R. (2011). Sub-persistence-length complex scaling behavior in lysozyme amyloid fibrils. Phys. Rev. Lett. *107*, 238101.

Larsen, P., Nielsen, J.L., Dueholm, M.S., Wetzel, R., Otzen, D., and Nielsen, P.H. (2007). Amyloid adhesins are abundant in natural biofilms. Environ. Microbiol. *9*, 3077–3090.

Lee, Y.J., Savtchenko, R., Ostapchenko, V.G., Makarava, N., and Baskakov, I.V. (2011). Molecular structure of amyloid fibrils controls the relationship between fibrillar size and toxicity. PLoS One *6*, e20244.

Li, D., Jones, E.M., Sawaya, M.R., Furukawa, H., Luo, F., Ivanova, M., Sievers, S.A., Wang, W., Yaghi, O.M., Liu, C., et al. (2014). Structure-based design of functional amyloid materials. J. Am. Chem. Soc. *136*, 18044–18051.

Lin, H.K., Boatz, J.C., Krabbendam, I.E., Kodali, R., Hou, Z., Wetzel, R., Dolga, A.M., Poirier, M.A., and van der Wel, P.C.A. (2017). Fibril polymorphism affects immobilized non-amyloid flanking domains of huntingtin exon1 rather than its polyglutamine core. Nat. Commun. *8*, 15462.

Lorenzen, N., Cohen, S.I., Nielsen, S.B., Herling, T.W., Christiansen, G., Dobson, C.M., Knowles, T.P., and Otzen, D. (2012). Role of elongation and secondary pathways in S6 amyloid fibril growth. Biophys. J. *102*, 2167–2175.

Mankar, S., Anoop, A., Sen, S., and Maji, S.K. (2011). Nanomaterials: amyloids reflect their brighter side. Nano Rev. *2*, 6032.

Marchante, R., Beal, D.M., Koloteva-Levine, N., Purton, T.J., Tuite, M.F., and Xue, W.F. (2017). The physical dimensions of amyloid aggregates control their infective potential as prion particles. Elife *6*, e27109.

Meinhardt, J., Sachse, C., Hortschansky, P., Grigorieff, N., and Fandrich, M. (2009). Abeta(1-40) fibril polymorphism implies diverse interaction patterns in amyloid fibrils. J. Mol. Biol. *386*, 869–877.

Milanesi, L., Sheynis, T., Xue, W.F., Orlova, E.V., Hellewell, A.L., Jelinek, R., Hewitt, E.W., Radford, S.E., and Saibil, H.R. (2012). Direct three-dimensional visualization of membrane disruption by amyloid fibrils. Proc. Natl. Acad. Sci. U S A *109*, 20455–20460.

Nicoud, L., Lazzari, S., Balderas Barragan, D., and Morbidelli, M. (2015). Fragmentation of amyloid fibrils occurs in preferential positions depending on the environmental conditions. J. Phys. Chem. B *119*, 4644–4652.

Paparcone, R., and Buehler, M.J. (2011). Failure of Abeta(1-40) amyloid fibrils under tensile loading. Biomaterials *32*, 3367–3374.

Peelaerts, W., Bousset, L., Van der Perren, A., Moskalyuk, A., Pulizzi, R., Giugliano, M., Van den Haute, C., Melki, R., and Baekelandt, V. (2015). alpha-Synuclein strains cause distinct synucleinopathies after local and systemic administration. Nature *522*, 340–344.

Robert, L., Hoffmann, M., Krell, N., Aymerich, S., Robert, J., and Doumic, M. (2014). Division in Escherichia coli is triggered by a size-sensing rather than a timing mechanism. BMC Biol. *12*, 17.

Romero, D., Aguilar, C., Losick, R., and Kolter, R. (2010). Amyloid fibers provide structural integrity to Bacillus subtilis biofilms. Proc. Natl. Acad. Sci. U S A *107*, 2230–2234.

Sachse, C., Grigorieff, N., and Fandrich, M. (2010). Nanoscale flexibility parameters of Alzheimer amyloid fibrils determined by electron cryo-microscopy. Angew. Chem. Int. Ed. *49*, 1321–1323.

Scior, A., Juenemann, K., and Kirstein, J. (2016). Cellular strategies to cope with protein aggregation. Essays Biochem. *60*, 153–161.

Shammas, S.L., Knowles, T.P., Baldwin, A.J., Macphee, C.E., Welland, M.E., Dobson, C.M., and Devlin, G.L. (2011). Perturbation of the stability of amyloid fibrils through alteration of electrostatic interactions. Biophys. J. *100*, 2783–2791.

Shorter, J., and Lindquist, S. (2004). Hsp104 catalyzes formation and elimination of self-replicating Sup35 prion conformers. Science *304*, 1793–1797.

Sondheimer, N., and Lindquist, S. (2000). Rnq1: an epigenetic modifier of protein function in yeast. Mol. Cell *5*, 163–172.

Steiner, J.A., Quansah, E., and Brundin, P. (2018). The concept of alpha-synuclein as a prion-like protein: ten years after. Cell Tissue Res. *373*, 161–173.

Surmacz-Chwedoruk, W., Malka, I., Bozycki, L., Nieznanska, H., and Dzwolak, W. (2014). On the heat stability of amyloid-based biological activity: insights from thermal degradation of insulin fibrils. PLoS One *9*, e86320.

Sweers, K.K., van der Werf, K.O., Bennink, M.L., and Subramaniam, V. (2012). Atomic force microscopy under controlled conditions reveals structure of C-terminal region of alpha-synuclein in amyloid fibrils. ACS Nano *6*, 5952–5960.

Tanaka, M., Collins, S.R., Toyama, B.H., and Weissman, J.S. (2006). The physical basis of how prion conformations determine strain phenotypes. Nature *442*, 585–589.

Tipping, K.W., van Oosten-Hawle, P., Hewitt, E.W., and Radford, S.E. (2015). Amyloid fibres: inert end-stage aggregates or key players in disease? Trends Biochem. Sci. *40*, 719–727.

Tornquist, M., Michaels, T.C.T., Sanagavarapu, K., Yang, X., Meisl, G., Cohen, S.I.A., Knowles, T.P.J., and Linse, S. (2018). Secondary nucleation in amyloid formation. Chem. Commun. (Camb) *54*, 8667–8684.

Tuite, M.F., and Serio, T.R. (2010). The prion hypothesis: from biological anomaly to basic regulatory mechanism. Nat. Rev. Mol. Cell Biol. *11*, 823–833.

Xue, W.F. (2013). Amyloid fibril length quantification by atomic force microscopy. In Bio-Nanoimaging Protein Misfolding & Aggregation, V.N. Uversky and Y.L. Lyubchenko, eds. (Academic Press), pp. 17–25.

Xue, W.F. (2015). Nucleation: the birth of a new protein phase. Biophys. J. *109*, 1999–2000.

Xue, W.F., Hellewell, A.L., Gosal, W.S., Homans, S.W., Hewitt, E.W., and Radford, S.E. (2009a). Fibril fragmentation enhances amyloid cytotoxicity. J. Biol. Chem. *284*, 34272–34282.

Xue, W.F., Homans, S.W., and Radford, S.E. (2008). Systematic analysis of nucleation-dependent polymerization reveals new insights into the mechanism of amyloid self-assembly. Proc. Natl. Acad. Sci. U S A *105*, 8926–8931.

Xue, W.F., Homans, S.W., and Radford, S.E. (2009b). Amyloid fibril length distribution quantified by atomic force microscopy single-particle image analysis. Protein Eng. Des. Sel. *22*, 489–496.

Xue, W.F., and Radford, S.E. (2013). An imaging and systems modeling approach to fibril breakage enables prediction of amyloid behavior. Biophys. J. *105*, 2811–2819.

Zeng, G., Vad, B.S., Dueholm, M.S., Christiansen, G., Nilsson, M., Tolker-Nielsen, T., Nielsen, P.H., Meyer, R.L., and Otzen, D.E. (2015). Functional bacterial amyloid increases Pseudomonas biofilm hydrophobicity and stiffness. Front. Microbiol. *6*, 1099.

iScience, Volume *23*

Supplemental Information

The Division of Amyloid Fibrils: Systematic Comparison of Fibril Fragmentation Stability by Linking Theory with Experiments

David M. Beal, Magali Tournus, Ricardo Marchante, Tracey J. Purton, David P. Smith, Mick F. Tuite, Marie Doumic, and Wei-Feng Xue

SUPPLEMENTARY FIGURES

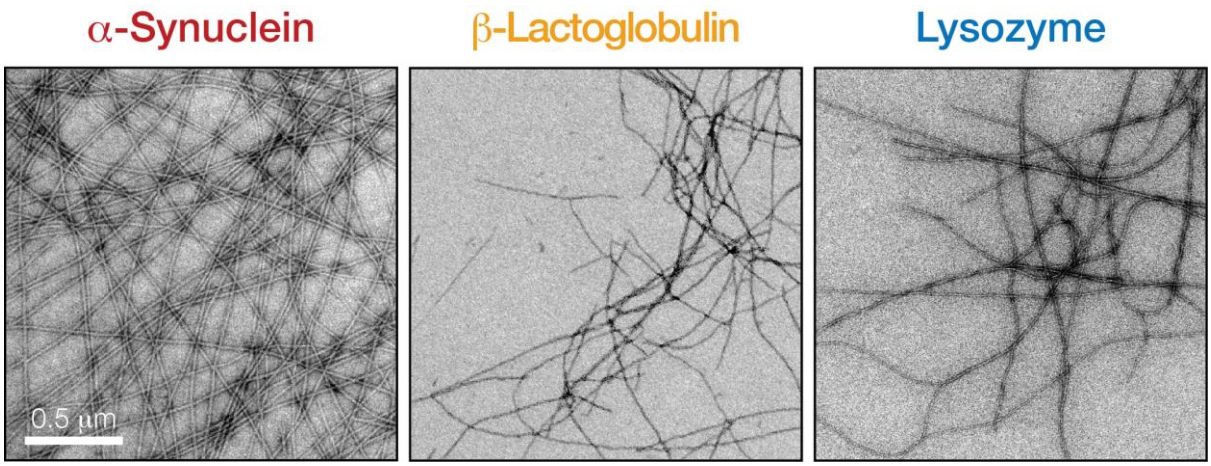

Supplementary Figure S1. Negative-stain TEM validation of the initial pre-formed amyloid fibril samples. Related to Figure 2. Initial human α-Syn, bovine milk β-Lac, and hen egg white Lyz amyloid fibril samples (all 120 µM monomer equivalent concentration) were deposited on glow-discharged, carbon coated Formvar copper grids and imaged using TEM after staining with 2% (w/v) uranyl acetate. Typical TEM images are shown with scale bar represents 500 nm in all images.

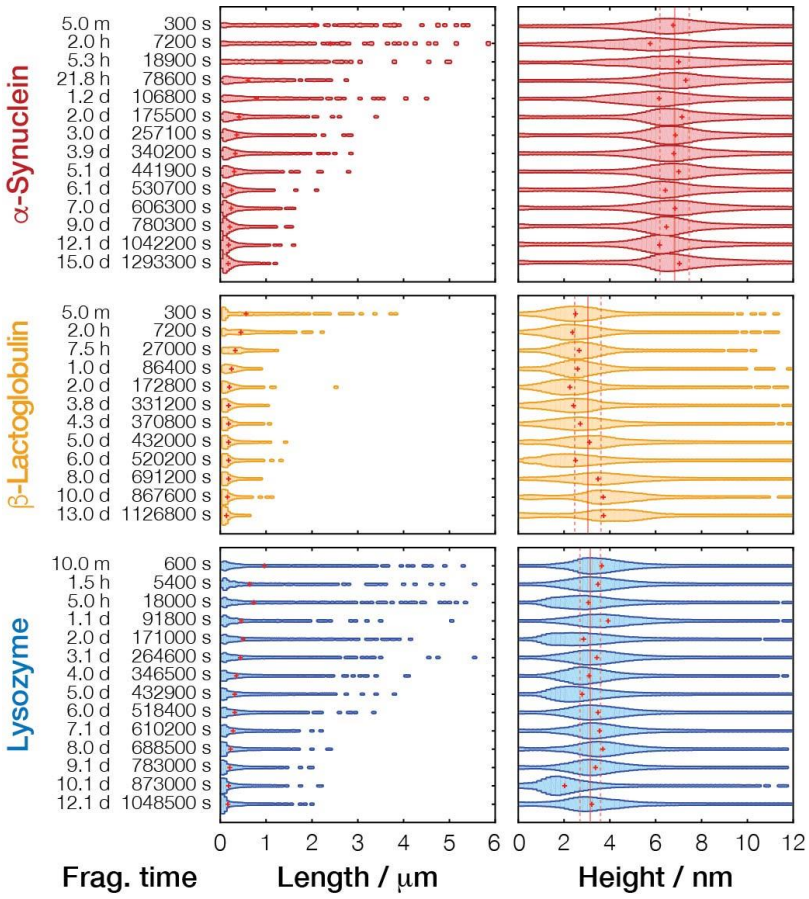

Supporting Figure S2. Fibril length and height distributions extracted from AFM images for fibrils undergoing fragmentation by mechanical stirring. Related to Figure 3. Typical experimental time course with normalized length (left plot of each sample) and height (right plot of each sample) distributions of fibril particles shown as violin plots. The width of the horizontal bars corresponds to the normalised frequencies observed at the length or height indicated by the x-axes. The bars for all samples are shown using the same length and height frequency scales, respectively, to facilitate comparison. The red crosses indicate mean values at each time point and the solid and dashed red lines for height plots indicate mean and standard deviation of all time points taken together, respectively.

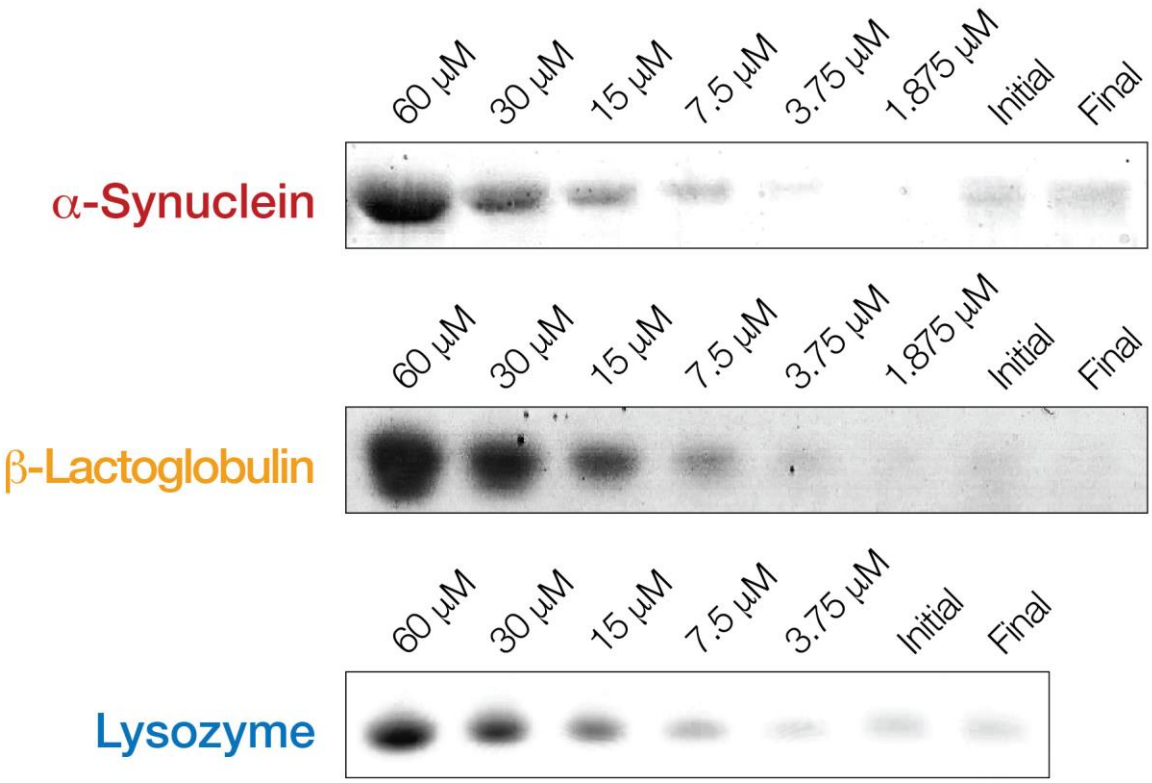

Supporting Figure S3: Residual monomer assay before and after fibril fragmentation time courses. Related to Figure 3. For each fibril type, protein content in the non-pellatable fractions of the initial sample before and Final sample after extended mechanical perturbation were visualised on SDS-PAGE gels together with loading standards of known protein concentrations. The difference in residual monomer concentration (difference between bands in the Initial and Final lanes) were less than 5 % in all cases.

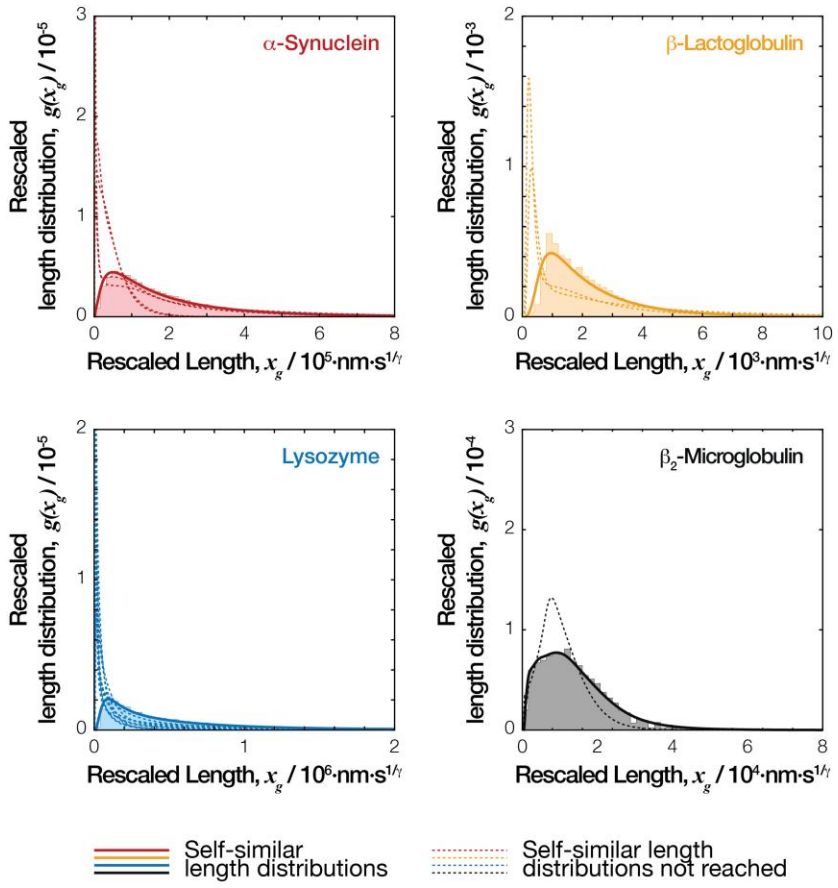

Supporting Figure S4: The self-similar length distribution shape can be obtained from rescaling and averaging of the experimental normalised length distributions. Related to Figure 5. The resealed length distributions $g(x_g)$ calculated with Eq. (5) are shown for each fibril type. For each fibril type analysed, the histograms and bold solid lines are the average of length distributions obtained from AFM imaging analysis that have reached the self-similar length distribution shapes, i.e. distributions at the time points consistent with Eq. (2) in the portion of the experiments represented by the solid lines in **Fig. 5**. for each fibril type. The dashed lines represent distributions from early experimental time-points where self-similarity has not been reached, demonstrating the large deviations from the self-similar distribution shape represented by the bold lines. The lines represent distributions calculated using the kernel density method to reduce clutter and facilitate visualisation and comparison.

SUPPLEMENTARY TABLE

Supporting Table S1: Sample, AFM imaging, and quantitative image analysis statistics. Related to Figure 2 and 3. Image analysis statistics for each sample and time point is shown. List of all raw fibril lengths is available upon request.

Samples		***AFM Imaging***			***Quantitative image Analysis***			
Protein	*Fragmentation Time /s*	*Number of Images*	*Image size / pixels*[†]	*Scan size / µm*[†]	*Mean Particle Length / nm*	*Number of Fibril Particles*[◊]	*Mean Particle Height / nm*	*Number of Pixels*[○]
α-Syn	300	6	2048	20	2075.8	653	6.8	49079
	7200	5	2048	20	2402.9	424	5.8	32066
	18900	3	2048	20	1311.6	679	7.0	43259
	78600	2	2048	20	598.9	1350	7.3	53512
	106800	2	2048	20	786.8	1512	6.1	63474
	175500	2	2048	20	406.2	3086	7.1	92632
	257100	2	2048	20	360.1	4087	6.8	110048
	340200	2	2048	20	330.6	4257	6.8	110024
	441900	2	2048	20	301.8	2723	7.0	67278
	530700	2	2048	20	244.7	5064	6.4	110431
	606300	2	2048	20	241.4	6104	6.8	129898
	780300	2	2048	20	208.9	6707	6.5	129581
	1042200	2	2048	20	185.6	6412	6.1	113509
	1293300	2	2048	20	173.6	5346	7.0	90832
	300	5	2048	20	2183.7	507	7.5	37725
	5400	5	2048	20	1756.2	394	7.0	24323
	18000	2	2048	20	1303.7	635	7.8	36938
	91800	2	2048	20	620.7	2293	7.2	87165
	107400	2	2048	20	568.5	2304	7.4	80443

	195900	2	2048	20	439.7	2416	7.2	77497
	259200	2	2048	20	390.5	3264	7.1	93323
	430500	2	2048	20	276.7	4807	6.9	114822
	610200	2	2048	20	224.3	6253	7.1	128690
	691200	2	2048	20	205.2	7541	6.8	145181
	766200	2	2048	20	194.0	5705	6.4	106589
	863700	2	2048	20	181.7	8086	6.5	143206
	1119600	2	2048	20	172.0	9532	6.4	161606
	1219800	2	2048	20	163.6	9470	6.3	154357
	1380900	2	2048	20	158.3	8811	6.8	139488
β-Lac	300	2	2048	20	560.2	496	2.5	28968
	7200	2	2048	20	451.8	854	2.4	40389
	27000	1	2048	20	329.7	751	2.7	26125
	86400	1	2048	20	244.7	1023	2.6	26678
	172800	1	2048	20	200.8	1482	2.3	32010
	331200	2	2048	20	183.0	2637	2.4	52129
	370800	1	2048	20	186.0	1112	2.7	22330
	432000	2	2048	20	185.2	2180	3.1	43588
	520200	2	2048	20	181.1	2190	2.5	42867
	691200	2	2048	20	181.0	1945	3.5	38036
	867600	1	2048	20	163.2	922	3.7	16349
	1126800	1	2048	20	134.2	1138	3.7	16819
	1800	3	2048	20	680.8	898	2.0	63514
	3600	2	2048	20	495.8	977	2.9	50594
	87588	1	2048	20	304.6	2649	3.1	85313
	107712	2	2048	20	310.3	2761	2.9	90538
	182376	3	2048	20	254.9	4664	2.9	126499
	437688	3	2048	20	236.1	3379	3.2	85122
	519876	2	2048	20	233.7	1957	3.6	48815
	624276	4	2048	20	229.9	3511	3.4	86233
	693000	2	2048	20	234.0	1752	3.7	43764
	777312	2	2048	20	237.0	1809	3.7	45739
	1058400	2	2048	20	230.0	830	3.7	20388
	1218960	2	2048	20	213.2	1465	3.2	33468

	1296000	3	2048	20	221.0	2109	3.5	49869
Lyz	300	3	2048	20	1436.6	437	3.1	38771
	1800	2	2048	20	364.7	632	3.4	18882
	3600	2	2048	20	881.6	750	3.1	35831
	7200	2	2048	20	1273.2	610	3.0	41984
	14400	2	2048	20	1103.4	519	3.1	35986
	28800	2	2048	20	1014.9	713	3.0	45954
	86400	2	2048	20	612.0	1500	3.5	79606
	172800	2	2048	20	333.6	2007	2.8	65634
	346600	2	2048	20	242.5	2592	2.9	64844
	432000	2	2048	20	211.3	4020	2.7	88812
	604800	1	2048	20	172.9	4270	2.8	78168
	1123200	2	2048	20	92.5	3419	2.6	35582
	600	3	2048	20	959.5	1402	3.6	69144
	5400	2	2048	20	591.9	1019	3.4	42686
	18000	2	2048	20	720.0	1125	3.0	55008
	91800	1	2048	20	448.8	541	3.9	20366
	171000	2	2048	20	495.9	1934	2.8	79284
	264600	3	2048	20	439.9	3423	3.4	133898
	346500	3	2048	20	351.2	4049	3.1	133400
	432900	3	2048	20	315.0	4798	2.8	145233
	518400	2	2048	20	313.9	3263	3.5	100009
	610200	1	2048	20	275.7	1452	3.5	39803
	688500	1	2048	20	223.1	2100	3.7	47373
	783000	1	2048	20	207.7	2082	3.3	44558
	873000	1	2048	20	181.7	3059	2.0	57672
	1048500	1	2048	20	164.3	2865	3.2	49244
β_2m*	540	16	1024	10	1002.0	468	5.9	36896
	3300	8	1024	10	746.8	515	5.4	29583
	8280	6	1024	10	616.2	650	5.5	29184
	16920	4	1024	10	506.6	603	5.7	22650
	39240	4	1024	10	380.2	859	4.6	25747
	84240	4	1024	10	301.7	1037	5.9	26177
	108000	4	1024	10	266.0	1298	4.8	28612

* Reanalysis of data from Xue and Radford, 2013

† Indicating scan size in μm x μm and image size in pixels x pixels as image aspect ratio was 1 throughout.

◊ Total number of fibril particles quantified for constructing the fibril length distributions.

° Total number of pixel height values in the fibril height distributions for fibril width evaluations.

THEORY

The self-similar division equation

We first explain here the origins of Eq. (1) in the Main Text as well as the assumptions associated with this equation. Let us denote the fibril length distribution *u(t, x)* as the particle concentration of fibrils of length x > 0 at time t, $B(x) \geq 0$ as the division rate constant for fibrils of length x (assumed to be independent of time), and $\kappa(y, dx)$ the probability that a dividing fibril of length y gives rise to two fibrils of size x and $y - x$ (Fig. 1b). The κ, often called fragmentation kernel, is nonnegative and satisfies the following properties:

$$\int_0^y \kappa(y, dx) = 1, \qquad \kappa(y, x > y) = 0, \qquad \kappa(y, x) = \kappa(y, y - x)$$

Eq. (S1)

The last property above is a symmetry property linked to the assumption that we consider only division into two daughter fibrils for each microscopic step, and the fibrils are isotropic along the axis of the filament so the division rate only depends on the length of the resulting two fibrils (**Fig. 1c** and **1d**). The first two properties of Eq. (S1) express that $\kappa(y, dx)$ is a normalised probability density function, and that daughter fibrils post-division are always shorter than their mother fibril. The time dependent concentration of fibrils *u(t, x)* then satisfies the following equation:

$$\frac{\partial}{\partial t}u(t,x) = -B(x)u(t,x) + 2\int_{y=x}^{\infty} \kappa(y,x)B(y)u(t,y)dy\,, \qquad u(0,x) = u_0(x)$$

Eq. (S2)

where $u_0(x)$ is the initial length distribution of fibrils. Equation (S2) is the continuous division equation, which describes the evolution $\frac{\partial}{\partial t}u(t,x)$ of the fibril particle concentrations in the fibril length

distribution *u(t, x)* with respect to time *t*. It states that fibrils of a given length *x* in the sample distribution will be consumed with a rate *B(x)* when they divide into smaller daughter fibrils, and that fibrils of the same length *x* may also appear in the sample distribution each time a fibril of size $y > x$ divides into two fibrils of size *x* and $y - x$. Let us denote the total initial mass of fibrils as $\rho = \int_0^\infty x u_0(x) dx$. Since the mass is conserved through time: $\int_0^\infty x u(t,x) dx = \rho$. We also assume, in line with previous theoretical (Hill, 1983) and experimental results (Xue and Radford, 2013), that the division rate constant is given by a power law:

$$B(x) = \alpha_0 (\alpha x)^\gamma, \qquad \alpha > 0, \qquad \gamma > 0$$

Eq. (S3)

and that the site where a fragmenting fibril of size *y* breaks down only depend on the relative position of its site along the mother fibril, defined by the ratio *x/y* where *x* is the length of one of the two daughter fibrils. This property is called a "self-similar" division and is translated mathematically with fragmentation kernel κ as the following:

$$\kappa(y,x) := \frac{1}{y} \kappa_0 \left(\frac{x}{y}\right)$$

Eq. (S4)

where the properties described by Eq. (S1), when transferred to the probability density κ_0, and with $z = \left(\frac{x}{y}\right)$, satisfies the following:

$$\int_0^1 \kappa_0(z) dz = 1, \qquad \kappa_0(z > 1) = 0, \qquad \kappa_0(z) = \kappa_0(1 - z)$$

Eq. (S5)

Two important examples may be viewed as special cases of self-similar fragmentation kernels above. The first one is the case of division of uniform probability: the parent fibril can break at any site along its length with an equal probability, so that $\kappa_0 \left(\frac{x}{y} \in (0,1)\right) = 1$. The second special division case is

sometimes referred to as the "equal mitosis case" from its roots in describing cellular divisions, where the parent fibril divides exactly at the middle, so that we have a Dirac delta function at $\kappa_0\left(\frac{1}{2}\right)$: $\kappa_0\left(\frac{x}{y}\right) = \delta_{\frac{x}{y}=\frac{1}{2}}$. Using all of the properties and assumptions above, the continuous division equation Eq. (S2) then becomes:

$$\frac{\partial}{\partial t}u(t,x) = -\alpha_0(\alpha x)^\gamma u(t,x) + 2\int_{y=x}^{\infty}\frac{1}{y}\kappa_0\left(\frac{x}{y}\right)\alpha_0(\alpha x)^\gamma u(t,y)dy$$

Eq. (S6)

which is equation Eq. (1) in the Main text.

Long-time behaviour of the continuous division equation

For our continuous division equation Eq. (1) and (S6), it has been proven in (Escobedo et al., 2005) that for long times, there exists a unique probability density function g and a constant $C_g > 0$ such that:

$$u(t,x) \underset{t\to\infty}{\longrightarrow} C_g t^{\frac{2}{\gamma}} g(x_g), \qquad x_g = x t^{\frac{1}{\gamma}}$$

Eq. (S7)

The constant C_g is introduced to ensure mass conservation, which holds for any time t. Eq. (S7) means that for large times, the probability density u tends towards a specific distribution shape g after variable rescaling. Moreover, the function g is defined as the unique solution to the following equation:

$$x_g\frac{dg(x_g)}{dx_g} + \left(2+\alpha\gamma x_g{}^\gamma\right)g(x_g) = 2\alpha\gamma\int_{y_g=x_g}^{\infty}\frac{1}{y_g}\kappa_0\left(\frac{x_g}{y_g}\right)y_g^\gamma g(y_g)dy_g\,, \qquad \int_0^\infty g(y_g)dy_g = 1$$

Eq. (S8)

We can then compute the constant C_g as the following:

$$\int_0^\infty xu(t,x)dx = \rho = C_g \int_0^\infty t^{\frac{2}{\gamma}} xg\left(xt^{\frac{1}{\gamma}}\right)dx = C_g \int_0^\infty x_g g(x_g)dx_g \quad \Longrightarrow \quad C_g = \frac{\rho}{\int_0^\infty x_g g(x_g)dx_g}$$

Eq. (S9)

We then relate these results to our experimental measurements. First, since we measure at successive time points small aliquots taken from the fibril samples, these samplings may be viewed as measurements of the length distribution of the fibril sample at time points *t*. We also do not measure directly *u(t, x)*, since the total number of fibrils is not known *a priori* for each time point. Instead, we measure the normalised length distribution *f(t, x)* as described below. Using Eq. (S7-S9), we then have the following:

$$\int_0^\infty u(t,x)dx \underset{t\to\infty}{\longrightarrow} C_g \int_0^\infty t^{\frac{2}{\gamma}} g\left(xt^{\frac{1}{\gamma}}\right)dx = C_g t^{\frac{1}{\gamma}} \int_0^\infty g(x_g)dx_g = C_g t^{\frac{1}{\gamma}}$$

Eq. (S10)

We can define $f(t,x)$ as the normalised fibril length distribution that can be assessed using the experimental image data:

$$f(t,x) = \frac{u(t,x)}{\int_0^\infty u(t,x)dx}$$

Eq. (S11)

Using this definition of *f(t, x)* from, we then have:

$$f(t,x) \underset{t\to\infty}{\longrightarrow} \frac{C_g t^{\frac{2}{\gamma}} g(x_g)}{C_g t^{\frac{1}{\gamma}}} = t^{\frac{1}{\gamma}} g(x_g), \qquad x_g = xt^{\frac{1}{\gamma}}$$

Eq. (S12)

which is equation Eq. (3) of the main text. Next, defining the average length of fibrils $\mu(t)$ as the experimentally tractable time-dependent mean length of the fibril length distribution defined as:

$$\mu(t) = \int_0^\infty x \cdot f(t,x)dx$$

Eq. (S13)

We have the following relationship:

$$\mu(t) := \int_0^\infty x f(t,x)dx \underset{t\to\infty}{\longrightarrow} \int_0^\infty x t^{\frac{1}{\gamma}} g\left(x t^{\frac{1}{\gamma}}\right) dx = t^{-\frac{1}{\gamma}} \int_0^\infty x_g g(x_g) dx_g = C t^{-\frac{1}{\gamma}},$$

$$C = \int_0^\infty x_g g(x_g) dx_g$$

Eq. (S14)

which is the relationship between the average length of fibrils and time t in equation Eq. (2) of the main text.

Estimating the division parameters α and γ

We first estimate γ by fitting a modified version of Eq. (2) to the average lengths $\mu(t)$ estimated from the experimentally observed fibril length distributions for sufficiently long times (see Eq. S22 in Transparent Methods). Then, we estimate α from γ and g using Eq. (S8). Integration of Eq. (S8) yields:

$$\int_0^\infty x_g \frac{dg(x_g)}{dx_g} dx_g + \int_0^\infty 2g(x_g)dx_g + \alpha\gamma \int_0^\infty {x_g}^\gamma g(x_g)dx_g = 2\alpha\gamma \int_0^\infty \int_{y_g=x_g}^\infty \frac{1}{y_g} \kappa_0\left(\frac{x_g}{y_g}\right) y_g^\gamma g(y_g) dy_g\, dx_g$$

Eq. (S15)

We can integrate Eq. (S15) by parts the first term, and we use Fubini's theorem to invert the integral order in the last term:

$$-\int_0^\infty g(x_g)dx_g + \int_0^\infty 2g(x_g)dx_g + \alpha\gamma \int_0^\infty {x_g}^\gamma g(x_g)dx_g = 2\alpha\gamma \int_0^\infty \int_{x_g=0}^{y_g} \frac{1}{y_g}\kappa_0\left(\frac{x_g}{y_g}\right) y_g^\gamma g(y_g)dx_g\, dy_g$$

Eq. (S16)

We then use the fact that g is normalised, $\int_0^\infty g(y_g)dy_g = 1$, and change the variable x_g to $z = \left(\frac{x_g}{y_g}\right)$ to obtain:

$$1 + \alpha\gamma \int_0^\infty {x_g}^\gamma g(x_g)dx_g = 2\alpha\gamma \int_0^\infty \int_{z=0}^{1} \kappa_0(z) y_g^\gamma g(y_g)dz\, dy_g$$

Eq. (S17)

Using the property $\int_0^1 \kappa_0(z)dz = 1$ from Eq. (S1), we obtain:

$$1 = \alpha\gamma \int_0^\infty {x_g}^\gamma g(x_g)dx_g$$

Eq. (S18)

To relate α directly to the experimentally characterised *f(t,x)* rather than on *g*, we multiply the equation Eq. (S12), i.e. Eq. (3) of the main text, by x^γ and integrate it to obtain the following:

$$\int_0^\infty x^\gamma f(t,x)dx \xrightarrow[t\to\infty]{} \int_0^\infty x^\gamma t^{\frac{1}{\gamma}} g\left(xt^{\frac{1}{\gamma}}\right)dx = \int_0^\infty x_g^\gamma t^{-1} g(x_g)dx_g$$

Eq. (S19)

Rearranging Eq. (S18) and using Eq. (S19), we obtain:

$$\alpha = \frac{1}{\gamma}\frac{1}{\int_0^\infty {x_g}^\gamma g(x_g)dx_g} \xrightarrow[t\to\infty]{} \frac{1}{\gamma}\frac{t^{-1}}{\int_0^\infty x^\gamma f(t,x)dx}$$

Eq. (S20)

Therefore, we get the following relationship:

$$\alpha \approx \frac{1}{\gamma} \frac{t^{-1}}{\int_0^\infty x^\gamma f(t,x)dx}, \qquad t \gg t_0$$

Eq. (S21)

which is used to estimate α from experimental data. For more details, we also refer the interested reader to Doumic et al., 2018, and more specifically to Lemma 1 and Eq. (3.3) in this reference.

TRANSPARENT METHODS

Preparation of protein monomers

Hen egg white Lyz and bovine β-Lac proteins were both purchased from Sigma-Aldrich and used with no further purification. Production and purification of human α-Syn monomers was achieved according to the method of Cappai et al (Cappai et al., 2005), with the addition of a stepped ammonium sulphate precipitation (30% to 50%) step prior to anion exchange chromatography. The protein was buffer exchanged using PD10 desalting column (GE Healthcare) prior to loading onto the anion exchange resin.

In vitro formation of amyloid fibril samples

The conversion of Lyz and β-Lac to amyloid fibres was achieved under acidic and heated conditions. Both proteins were dissolved in 10 mM HCl to a concentration of 15mg/ml and then incubated for 4 hr at 25 °C. The resulting solutions were filtered through a 0.2 μm syringe filter and diluted to a concentration of 10mg/ml (Lyz = 699 μM and β-Lac = 547 μM). 500 μl aliquots were then heated without agitation for differing periods of time, with Lyz heated at 60 °C for 2 days and β-Lac heated at 90 °C for 5 hr. α-Syn fibrils were formed by buffer exchange of purified monomers into fibril forming buffer (20mM Sodium phosphate, pH7.5) using a PD-10 column (GE Healthcare). The resulting α-Syn solution was passed through a 0.2 μm syringe filter. Protein concentration was subsequently determined via absorbance at 280nm, and the sample solution were diluted to 300 μM and incubated at 37 °C in a shaking incubator with agitation set at 200 rpm for at least two weeks.

Controlled fibril fragmentation through mechanical perturbation

Parent fibril solutions were diluted to 120 μM using the appropriate fibril forming buffer for each protein in a snap cap vial containing an 8 x 3 mm PTFE coated magnetic stirrer bar and then subjected to stirring at 1000 rpm on an IKA squid stirrer plate with digital speed display. At appropriate time points, small aliquots of the fibril samples were removed, diluted with fibril forming buffer (deposition concentration for α-synuclein is 0.48 μM, β-lactoglobulin is 0.6 μM and Lyz is 6 μM), and 20 μl were immediately taken and incubated for 5 min on freshly cleaved mica surfaces (Agar Scientific F7013). The mica surfaces were subsequently washed with 1 ml of syringe filtered (0.2 μm) mQ H_2O and dried under a gentle stream of N_2(g).

Determination of residual monomer concentration

Residual monomer concentration for each fragmentation sample were measured using SDS-PAGE after centrifugation (75000 rpm, 15 min) with 100 μl of the 120 μM fragmentation reaction and 100 μl of 120 μM non-fragmented parent fibrils samples. The top 10μl of the solutions were then removed and treated with 4x loading dye and boiled at 95 °C for 5 min (Lyz samples were heated to 65 °C and beta-mercaptoethanol was not added due to decomposition of samples). The samples were then run against a serial dilution of monomeric protein standards on either a Tris-Tricine gel or a 15% Tris-Glycine gel at 180V and subsequently stained with Coomassie blue. Analysis of the protein bands was carried out by densitometry for comparison of bands to the serial dilution bands.

AFM imaging and image analysis

The fibril samples were imaged on a Bruker Multimode 8 scanning probe microscope with a Nanoscope V controller, using the ScanAsyst peak-force tapping imaging mode. Bruker ScanAsyst probes (Silicone nitride tip with tip height = 2.5-8 μm, nominal tip radius = 2 nm, nominal spring constant 0.4 N/m and nominal resonant frequency 70 kHz) were used throughout. Multiple 20 μm x 20 μm areas of the surface were scanned at a resolution of 2048 x 2048 pixels. The images were then processed and flattened using Bruker Nanoscope Analysis software to remove tilt and bow. The images were then

imported into Matlab, where length of individual fibril particles was measured. The sample length and height distributions were obtained as previously described (Xue, 2013; Xue et al., 2009). For the fibril length distributions, any length-dependent bias in a deposition for imaging or during the fibril tracing step of image analysis was taken into account as previously described (Xue et al., 2009).

Data analysis of fibril division properties

The normalised length distribution of the fibril samples measured by AFM at time *t*, $f(t,x)$, is linked to the concentration of fibrils solution $u(t,x)$ in Eq. (1) by the relation in Eq. (SI.11). Mean lengths for each time point $\mu(t)$ were calculated from the experimental $f(t,x)$ distributions and Eq. (2) and (4) where used to first extract γ from the datasets. Because some unknown number of experimentally measured length distributions at early time points in the experiments may not have sufficiently reached the self-similar distribution at the asymptotic line (i.e. where Eq. (2) does not apply), we fit the following equation Eq. (4) to the average length as function of time data instead of Eq. (2) directly in order to estimate the number of experimental time points consistent with the self-similar distribution shape objectively without human input:

$$\begin{cases} \mu(t) = C \cdot t^{-1/\gamma}; & t > t_s \\ \mu(t) = C \cdot {t_s}^{-1/\gamma}; & t \leq t_s \end{cases}$$

Eq. (S22)

Eq. (4) was fit to the average length $\mu(t)$ as function of time *t*, with *C* and t_s as parameters individual to each experimental dataset and γ as a global parameter for datasets from the same fibril type. Subsequently, the $g(x_g)$ and α values were calculated with Eq. (3) and (SI.21), respectively, both using γ calculated above and experimental normalised length distributions $f(t,x)$ where $t > t_s$. For both the $g(x_g)$ distributions and α values, averages were obtained for each fibril type. The self-similar distribution shapes $g(x_g)$ were used to calculate length distribution at any time using the reverse of Eq. (3). The α and γ values were used to calculate the division rate constant $B(x) = \alpha_0(\alpha x)^\gamma$ for fibrils of

any length x. Supplementary information section contains further information on the mathematical considerations of our division model.

Direct numerical simulation of fibril division processes

To validate the α and γ values obtained from our analysis, direct numerical simulations to calculate the time evolution of the fibril length distributions were carried out by numerically solving the full ODE system describing the master equation mostly as described in Xue and Radford, 2013 but with a few modifications. Firstly, numerical integrations of the master equation were solved for fibril species containing up to 30,000 instead of 20,000 monomeric units in order to retain concentration errors introduced by numerical inaccuracy and truncation of larger species to <1%. Secondly, the number of division sites was assumed to be equal to the number of monomers-1 and the unit used for the length of fibrils was interconverted in the simulations from nanometres (x in [nm] units) to the number of monomers (i number of monomers) using the numbers of monomers per nm length unit N_l (Xue and Radford, 2013) as conversion factor. Subsequently, assuming that division sites along the fibrils operate independently, the microscopic rate constant on per division site basis is $B(i)\kappa_0$ divided by the number of monomers-1. Thirdly, as $g(x_g)$ shape for Lyz and α-Syn fibril divisions suggest a κ_0 function that result in similar division rates in the fibril centre and fibril edge, simulations for these two fibril types were carried out using Eq. S6 in Xue and Radford 2013 instead of Eq. S8. Finally, the experimental distribution at the first time-points (including all the experimental noise) were directly used as the initial distribution (dashed lines in **Fig. 6**) instead of parameterised distributions (Xue et al., 2009) in the simulations to illustrate the fact that our model has shown that the self-similar distribution shape will be reached independently of the initial length distribution.